

**EXPERIMENTAL AND NUMERICAL INVESTIGATION OF
AN S-DUCT DIFFUSER THAT IS DESIGNED FOR
A MICRO TURBOJET ENGINE POWERED AIRCRAFT**

**A THESIS SUBMITTED TO
THE GRADUATE SCHOOL OF NATURAL AND APPLIED SCIENCES
OF
MIDDLE EAST TECHNICAL UNIVERSITY**

BY

SAMET ASLAN

**IN PARTIAL FULFILLMENT OF THE REQUIREMENTS
FOR
THE DEGREE OF MASTER OF SCIENCE
IN
AEROSPACE ENGINEERING**

JANUARY 2017

Approval of the thesis:

**EXPERIMENTAL AND NUMERICAL INVESTIGATION OF
AN S-DUCT DIFFUSER THAT IS DESIGNED FOR
A MICRO TURBOJET ENGINE POWERED AIRCRAFT**

submitted by **SAMET ASLAN** in partial fulfillment of the requirements for the degree of
**Master of Science in Aerospace Engineering Department, Middle East Technical
University** by,

Prof. Dr. Gülbin Dural Ünver

Dean, Graduate School of **Natural and Applied Sciences**

Prof. Dr. Ozan Tekinalp

Head of Department, **Aerospace Engineering**

Assoc. Prof. Dr. D. Funda Kurtuluş

Supervisor, **Aerospace Engineering Dept., METU**

Examining Committee Members:

Prof. Dr. Serkan Özgen

Aerospace Engineering Dept., METU

Assoc. Prof. Dr. Dilek Funda Kurtuluş

Aerospace Engineering Dept., METU

Prof. Dr. Nuri Yücel

Mechanical Engineering Dept., Gazi University

Asst. Prof. Dr. Nilay Sezer Uzol

Aerospace Engineering Dept., METU

Asst. Prof. Dr. Kutluk Bilge Arıkan

Mechatronics Engineering Dept., Atılım University

Date: 12/01/2017

I hereby declare that all information in this document has been obtained and presented in accordance with academic rules and ethical conduct. I also declare that, as required by these rules and conduct, I have fully cited and referenced all material and results that are not original to this work.

Name, Last Name: SAMET ASLAN

Signature:

ABSTRACT

EXPERIMENTAL AND NUMERICAL INVESTIGATION OF AN S-DUCT DIFFUSER DESIGNED FOR A MICRO TURBOJET ENGINE POWERED AIRCRAFT

Aslan, Samet

M.S., Department of Aerospace Engineering

Supervisor: Assoc. Prof. Dr. D. Funda Kurtulus

JANUARY 2017, 72 pages

S-duct diffusers are often used for aircraft propulsion systems that convey the intake air to the engine compressor. In this thesis, flow structure at separated entrance conditions in an S-duct diffuser that designed for a micro turbojet engine powered aircraft is investigated using experimental and numerical methods. Flow characteristics such as flow separation, secondary flows, and swirl are investigated to find out the source of distortions and pressure loss at aerodynamics interface plane.

Experiments are performed at three different mass flow rates at TEI test facility. Measurements of total pressures and static pressures are obtained at the aerodynamic interface plane (AIP). Also, wall static pressures through the duct are measured. Results show that stream wise flow separation is occurred within the duct. Total pressure loss is seen as a result of the flow structure. Total pressure loss is seen to increase with increasing mass flow rate. Furthermore, circumferential distortion is also examined.

Flow structure in a short S-duct diffuser at representative cruise conditions is numerically investigated for validation of simulations. Computations are compared with the experimental data obtained from literature. The results are

found to compare well with experiment. Spalart-Almaras turbulence model gives the most suitable results considering mass flow rate, Mach number and pressure recovery values together.

The experiment that performed at TEI is simulated and results are compared with the experimental data. RANS equations are solved with Ansys Fluent 14 commercial CFD code. Various turbulence models are used and their efficiencies are compared. Furthermore, effect of the inlet boundary profile is surveyed. Lip separation is seen at the entrance of the S-duct. Also, streamwise flow separation regions were caught through the bends of the diffuser. It is found that lip separation strengthen the effect of the wall separations inside the duct and increases the AIP distortion drastically.

Numerical analyses approach the experimental wall pressure values considerably well. Reynolds Stress Model gives the closest results to the ones experimentally obtained. However, RANS solutions overpredict the pressure loss and pressure gradient across the AIP. Afterwards, transient analyses are performed for the same case using URANS and SAS approaches. While results of URANS computations are almost identical with RANS results, SAS analyses provide impressive improvement especially for predicting distortion.

Keywords: S-duct Diffuser, S-duct Inlet, Serpentine Inlet, Intake Aerodynamics, Flow Separation, Swirl, Pressure Recovery, Distortion, Surge, Thrust, Specific Fuel Consumption

ÖZ

MİKRO TURBOJET MOTORLU BİR UÇAK İÇİN TASARLANMIŞ BİR S-KANAL DİFÜZÖRÜN DENEYSEL VE NÜMERİK YÖNTEMLERLE İNCELENMESİ

Aslan, Samet

Yüksek Lisans, Havacılık ve Uzay Mühendisliği Bölümü

Tez Yöneticisi: Assoc. Prof. Dr. D. Funda Kurtuluş

Ocak 2017, 72 sayfa

S-kanal difüzörleri, giriş havasını motor kompresörüne iletmede uçak itki sistemleri için sıklıkla kullanılır. Bu tezde, mikro turbojet motorlu bir uçak için tasarlanmış bir S kanallı difüzörde ayrılmış giriş koşullarında akış yapısı, deneysel ve sayısal yöntemler kullanılarak incelenmiştir. Aerodinamik arayüz düzlemindeki bozulma ve basınç kaybının kaynağını bulmak için akış ayrılması, ikincil akışlar ve girdap gibi akış özellikleri araştırılmıştır.

Deneyler, TEI test tesisinde üç farklı kütle debisinde gerçekleştirilmiştir. Aerodinamik ara yüz düzleminde (AIP) toplam basınç ve statik basınç ölçümleri alınmıştır. Ayrıca kanal üzerinden duvar statik basınçları ölçülmüştür. Sonuçlar kanal içinde akış doğrultusunda ayrılmanın meydana geldiğini göstermektedir. Akış yapısının sonucu olarak toplam basınç kaybı görülmüştür. Toplam basınç kaybı, artan kütle debisi ile artmaktadır. Ayrıca, çevresel bozulma da incelenmiştir.

Simülasyonların doğrulanması için temsili seyir koşullarındaki kısa bir S-kanal difüzördeki akış yapısı sayısal olarak araştırılmıştır. Hesaplamalar literatürden elde edilen deneysel verilerle karşılaştırılmıştır. Sonuçların deneyle örtüştüğü tespit edilmiştir. Spalart-Almaras türbülans modeli, kütle akış hızı, Mach sayısı

ve basınç geri kazanım değerlerini birlikte ele alındığında en uygun sonuçları vermiştir.

TEI'de yapılan deney simule edilmiş ve sonuçlar deney verileri ile karşılaştırılmıştır. RANS denklemleri Ansys Fluent 14 ticari CFD kodu ile çözülmüştür. Çeşitli türbülans modelleri kullanılmış ve verimlilikleri karşılaştırılmıştır. Ayrıca, giriş sınır profilinin etkisi araştırılmıştır. S-kanal girişinde dudak ayrılması görülmüştür. Ayrıca, difüzörün dönüşleri boyunca akış doğrultusunda ayrılma bölgeleri yakalanmıştır. Dudak ayırmanın kanal içindeki duvar ayrılmalarının etkisini güçlendirdiği ve AIP bozulmasını büyük ölçüde arttırdığı bulunmuştur.

Sayısal analizler, deneysel duvar basınç değerlerine oldukça iyi yaklaşmaktadır. Reynolds Stres Modeli deneysel olarak elde edilen sonuçlara en yakın sonuçları vermiştir. Bununla birlikte, RANS çözümleri AIP boyunca basınç kaybı ve basınç gradyenini olduğundan yüksek tahmin etmektedir. Daha sonra, URANS ve SAS yaklaşımlarını kullanarak aynı vaka için geçici analizler gerçekleştirilmiştir. URANS hesaplamaları sonuçları RANS sonuçları ile hemen hemen aynı olmakla birlikte, SAS analizleri özellikle bozulmayı öngörmede etkileyici bir iyileşme sağlamaktadır.

Anahtar Kelimeler: S-kanal Difüzör S-kanal Hava Alığı, Serpantin Hava Alığı, Hava Alığı Aerodinamiği, Akış Ayrılması, Girdap, Basınç Korunumu, Bozuntu, Dalgalanma (surge), İtki, Özgül Yakıt Tüketimi

To My Family

ACKNOWLEDGMENTS

I wish to express my deepest gratitude to my supervisor Assoc. Prof. Dr. D. Funda Kurtuluş for her guidance, advice, criticism, encouragements and insight throughout the thesis.

I would also like to thank Dr. Erinç Erdem, Asst. Prof. Dr. Tolga Yasa for their suggestions, comments and also my colleagues in Test and Validation Team of TEI for all their help and friendship during the research.

I want to express best wishes to Sefa Yılmaztürk, Ender Hepkaya, Bertan Kaynaroğlu, Umut Can Küçük, and İsa Kavas for their friendship and support during this study.

I owe special and deepest gratitude to my parents Fatma Aslan, Yahya Aslan for their love, support, patience and encouragement throughout the study.

TABLE OF CONTENTS

ABSTRACT	V
ÖZ	VII
ACKNOWLEDGMENTS	X
LIST OF TABLES	XIII
LIST OF FIGURES	XIV
LIST OF SYMBOLS.....	XVII
CHAPTERS	
1 INTRODUCTION 1	
1.1. Motivation	1
1.2. Objective	3
1.3. Thesis Overview	3
2 THEORETICAL BACKGROUND 5	
2.1. Inlet Flow Characteristics.....	5
2.2. Effects of Inlet Performance on Engine	8
2.3. Inlets at Incidence.....	10
2.4. Literature Study.....	11
3 EXPERIMENTAL SETUP AND RESULTS 17	
3.1. Test Section	17
3.2. S-duct Inlet	19
3.3. Instrumentation.....	19
3.4. Data Reduction	22
3.5. Experimental Results.....	25
4 VALIDATION STUDY FOR NUMERICAL SIMULATIONS 29	
4.1. Case Definition.....	29
4.2. M2129 Diffuser Geometry	30
4.4. Grid Generation.....	32
4.5. Boundary Conditions.....	33
4.6. CFD Flow Solver	34
4.7. Turbulence Modeling	34

4.8.	Results	35
5	NUMERICAL INVESTIGATION OF THE S-DUCT DIFFUSER FLOW STRUCTURE	
	41	
5.1.	Case Definition	41
5.2.	Numerical Approach.....	41
5.3.	Results	44
6	NUMERICAL INVESTIGATION OF THE TRANSIENT FLOW STRUCTURE IN S-DUCT DIFFUSER	
	55	
6.1.	Numerical Approach.....	55
6.2.	Boundary Conditions	56
6.3.	Turbulence Modeling.....	56
6.4.	Results	57
7	CONCLUSION	65
REFERENCES:		69

LIST OF TABLES

TABLES

Table 3.1: Geometrical Parameters Defining the Test Section.....	18
Table 3.2: Geometrical Parameters Defining the S-duct Model.....	19
Table 3.3: Instrument Properties.....	22
Table 3.4: Mass Flow Rates.....	22
Table 3.5: Performance Parameters.....	26
Table 4.1: Geometrical Parameters Defining the RAE M2129 S-duct Diffuser Model.....	31
Table 4.2: Boundary Conditions.....	33
Table 4.3: Mesh Size and y^+ Relation.....	35
Table 4.4: Analyses Conditions.....	36
Table 4.5: Comparison of Numerical and Experimental Data.....	39
Table 5.1: Mesh Size and y^+ Relation.....	42
Table 5.2: Turbulence Model Study Analyses Properties.....	47
Table 5.3: Performance Parameters.....	52
Table 6.1: Performance Parameters.....	63

LIST OF FIGURES

FIGURES

Figure 2.1: Representative S-duct Geometry.....	6
Figure 2.2: Effect of Centrifugal Forces.....	8
Figure 2.3: Representative Compressor Map.....	9
Figure 2.4: Maneuver Envelope of YF16 Aircraft at Subsonic and Supersonic Speeds.....	10
Figure 2.5: S-duct Flow Separation and Lip Separation.....	11
Figure 3.1: Schematic View of the Test Setup.....	18
Figure 3.2: Schematic View of the S-duct Inlet.....	19
Figure 3.3: Instrumentation and Test Section.....	20
Figure 3.4: 2D Linear Traverse System Configuration.....	20
Figure 3.5: AIP Measurement Locations.....	21
Figure 3.6: Illustration of Total Pressure Contours and θ Sector for Definition of Distortion Coefficient.....	24
Figure 3.7: Top Wall GPR through the Duct.....	25
Figure 3.8: Bottom Wall GPR through the Duct.....	25
Figure 3.9: Incompressible Flow Ratio η_{σ_i} Contours at AIP.....	26
Figure 4.1: M2129 Diffuser Geometry.....	30

Figure 4.2: Mesh Structure.....	33
Figure 4.3: Contour Plots for Analysis (1, 2, 3, 4, 5).....	38
Figure 4.4: Experimental Pressure Recovery Contour at the Outlet Plane.....	38
Figure 5.1: Mesh Structure.....	43
Figure 5.2: Top Wall GPR through the S-duct Diffuser for Grid Optimization.....	44
Figure 5.3: Bottom Wall GPR through the S-duct Diffuser for Grid Optimization.....	45
Figure 5.4: Symmetry Plane Streamlines and Outlet η_{σ_i} Contours for Grid Optimization.....	46
Figure 5.5: Top Wall GPR through the S-duct Diffuser for Different Turbulence Models and BCs.....	47
Figure 5.6: Bottom Wall GPR through the S-duct Diffuser for Different Turbulence Models and BCs.....	48
Figure 5.7: Symmetry Plane Streamlines and Outlet η_{σ_i} Contours for Different Turbulence Models and BCs.....	50
Figure 5.8: Experimental η_{σ_i} Contour at the Outlet Plane.....	51
Figure 6.1: Symmetry Plane Streamlines and η_{σ_i} Contours of URANS Analyses.....	57
Figure 6.2: Mass flow rate (\dot{m}/\dot{m}_{\max}) history.....	58
Figure 6.3: Top Wall GPR through the S-duct Diffuser.....	58
Figure 6.4: Bottom Wall GPR through the S-duct Diffuser	59

Figure 6.5: Instantaneous Symmetry Plane Streamlines and Outlet η_{σ_i} Contours at Different Times.....	61
Figure 6.6: η_{σ_i} Contours of SAS Analyses and Experiment.....	61

LIST OF SYMBOLS

X	Engine thrust, N
P_{∞}	Freestream pressure, Pa
ΔP	Pressure difference, Pa
CFD	Computational fluid dynamics
M	Mach number
Re	Reynolds number
AIP	Aerodynamic interface plane
A	Area, m^2
D	Diameter, m
H	Height of S-duct diffuser, m
L	Length of S-duct diffuser, m
s	Length of S-duct diffuser centerline, m
m	Meter
\dot{m}	Mass flow rate, kg/s
P	Total pressure, Pa
p	Static pressure, Pa
q	Dynamic pressure, Pa
P_{amb}	Ambient Pressure, Pa

Pa	Pascal
GPR	Gauge pressure ratio
PR	Pressure recovery
η_{σ_i}	Incompressible flow ratio
$DC(\theta)$	Distortion parameter
θ	Distorted region angle, °
°	Degree
exp	Experimental
LES	Large eddy simulation
RANS	Reynolds averaged Navier Stokes
RKE	Realizable k-epsilon model
EWf	Enhanced wall function
RSM	Reynolds Stress Model
SST	Shear stress transport
SA	Spalart-Almaras
URANS	Unsteady Reynolds averaged Navier Stokes
SAS	Scale adaptive simulation
y^+	Dimensionless wall distance
α	Pitch angle, °
β	Sideslip angle, °
uni	Uniform

BC	Boundary condition
\vec{V}	Velocity, m/s
u	Velocity component in x direction, m/s
v	Velocity component in y direction, m/s
w	Velocity component in z direction, m/s
V'	Nondimensional velocity, V/V_{maz}
τ	Shear stress, Pa
f	Body force per unit mass
e	Internal energy per unit mass
\dot{q}	Rate of volumetric heat addition per unit mass
T	Temperature, °C
k	Thermal conductivity

CHAPTER 1

INTRODUCTION

1.1. Motivation

As the first element of a propulsion system, an inlet prepares the working conditions for the engine. It has got a critical importance for the engine performance and safety throughout the flight. The role of an inlet is to slow down the incoming airflow, by converting as much of the airflow kinetic energy as possible into static pressure at the compressor face. Since an inlet provides the air for the engine, it is supposed to be designed for the optimum engine operation. However, there are other concerns besides engine performance that influence the inlet design.

Missiles and military aircrafts are not expected to be identifiable during their missions. Rotating blades are the most vulnerable parts to radar signals. Therefore, putting the engine inside of the aircraft, hence outside of the reach of direct radar signals, is the fundamental approach to gain good stealth properties. When the engine is located inside of the fuselage, serpentine inlets are needed to convect air from the external flow into the engine interface. Therefore, S-duct inlets became a critical aspect for aircraft design, because, they let the engine to be buried in the fuselage and make the aircraft less visible to radar by preventing the engine face from direct radar signals ([1]-[4]).

Moreover, submergence of the engine inlet reduces the inlet ram drag as compared to a conventional pylon-mounted engine. The elimination of the

pylon also results in a decrease in weight due to the removal of the required supporting structure ([4], [5]).

Due to the mentioned reasons, the use of serpentine inlets in aerospace industry is rapidly increasing lately. They are chosen especially by defense industry for missile and military aircraft designs. The reason behind their popularity is to reduce the aircraft observability and mass, and to increase the volume of fuel tanks by using serpentine inlets. Regarding this trend inherent geometrical shape is getting more and more constrained to be short and compact, resulting in high exit to entrance area ratio. These two sets of constraints are clearly conflicting: curved and short inlets that decrease the system observability and respect compactness constraints cause loss of efficiency. On the other hand, the improvement in the flow properties given by a longer, less curved inlet increases the propulsive efficiency of the system and leads to higher vehicle thrust and better maneuverability. Inlet length and compactness on one hand and airflow quality on the other hand have to be traded when designing these types of inlets. S-duct air inlets, which represent a decent compromise, are very commonly used on cruise missiles ([4], [6]).

The flow in S-duct air inlets has been widely studied ([5], [29]). Longitudinal and circumferential static pressure gradients were found to be generated due to the bends. It was shown that they are subject to boundary layer separation and secondary flows, because of their particular shape. This leads to a total pressure loss, distortion and instabilities at the compressor face, which can translate into stall and consequently surge of the engine. The performance of the inlet can get worsen when the inlet is subjected to off-design external conditions, such as those that can occur when the aircraft is maneuvering. In the case of high angle of attack and high-g maneuvers large separations can occur leading to considerable pressure losses as well as high compressor face distortion, with much increased risk of compressor instabilities.

1.2. Objective

The objective of this thesis is to investigate aerodynamic characteristics of an S duct diffuser that is designed for a micro turbojet engine powered aircraft using experimental and numerical methods

Flow characteristics such as separation regions, the extend and magnitude of secondary flows, and associated swirl are investigated to find out the source of distortions and pressure loss at aerodynamics interface plane. Experiments are performed with the instrumented S-duct diffuser. The numerical simulations are validated with experimental data that is found in literature for an S-duct inlet at representative cruise conditions. Furthermore, studied test case is investigated with numerical methods.

1.3. Thesis Overview

Chapter 2 provides a detailed description of theoretical background for both experimental and numerical studies. Details of the test setup are provided in Chapter 3. Chapter 4 addresses the validation of numerical methods using a study of a different S-duct diffuser that is found in literature. Chapter 5 shows the numerical analyses of the test case described in Chapter 3. In this chapter grid refinement study is performed and the effect of the turbulence model is investigated. Moreover, the impact of the entrance conditions on flow structure is examined. In Chapter 6 the same test case is analyzed using unsteady numerical methods. Chapter 7 provides a summary of the experimental and numerical results and conclusions.

CHAPTER 2

THEORETICAL BACKGROUND

2.1. Inlet Flow Characteristics

Inlet or intake is an aircraft component that provides air to the airbreathing engines from the atmosphere. Flow around the aircraft also goes over the inlet and influenced by its presence. The internal flow enters the inlet and it has a critical importance for engine performance and stability [1].

What is expected from an inlet is stated in General Electric Company Installation Handbook for Turbojet Engines [3], as; “This process must be accomplished with the least possible loss in total-pressure or head, with the best attainable flow distribution, and with the least amount of drag.”

High pressure recovery through the inlet is required for high thrust levels and generally it is considered to represent the efficiency of the diffuser. Engine thrust directly depends on the inlet pressure recovery as in equation (2.1):

$$\frac{\Delta X}{X} = K \frac{\Delta P}{P_{\infty}} \quad (2.1)$$

where X is engine thrust, K is an empirical coefficient that depends upon the particular engine.

Beside high pressure recovery, the flow is also must be quality compatible for smooth and stable engine operation. This means that the flow entering to the compressor should be as uniform as possible.

Distortion is defined as the variation from this ideal uniform flow structure. In addition flow angularity in the aerodynamic interface plane (AIP), that is, the deviation of the flow direction from the axial engine direction is a further distortion parameter called swirl ([1], [2], [8]).

The throughflow projection of the centerline of S-shaped ducts consists of 1 S-like bend, between two straight parts (Figure 2.1). In this respect, the geometry of an S-duct is described by the evolution of its S-shape centerline and of its cross section form and area ([4], [8]). Although the S-ducts are advantageous as mentioned, they come with a price. If the length of the duct is short and/or the adverse pressure gradient induced by area increase is high, severe separation region appears in the upstream part of the S-duct, the flow subsequently relaxing in the aft part.

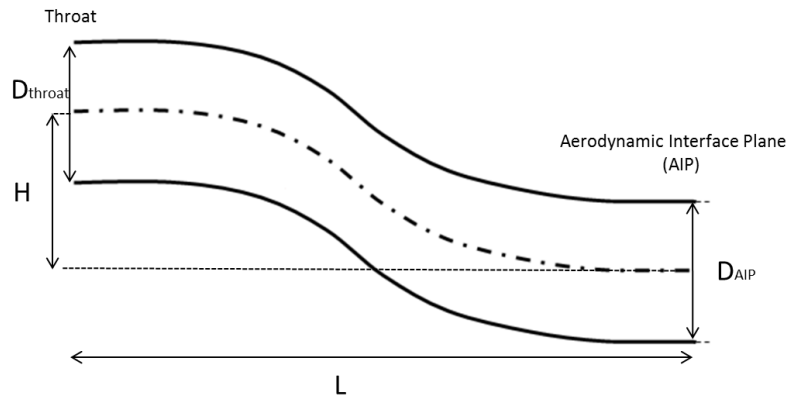


Figure 2.1: Representative S-duct Geometry

Wall friction, turbulent mixing and shock waves cause total pressure loss inside the duct. As the internal flow is being retarded, adverse pressure gradient affects the boundary layer. This is resulted in flow separation and turbulent mixing ([1], [2]).

Circumferential distortion directly influences the compressor operation. As total pressure distortion increases operating point moves towards to the surge line ([5]-[7]).

Flow separations and wake are the primary sources of total pressure distortion. Lip and sidewall separations can also be seen inside of the duct. As a result of high diffusion rates, boundary layer may thicken and even separate at the inner side of the bends. Due to increasing cross sectional area, adverse streamwise pressure gradient appears and this also causes flow separation. Drastic changes occur in local flow conditions at the separation regions. Moreover, shock and boundary layer interactions create inlet distortion at supersonic flight conditions ([7]-[9]).

Flow structure in a curved pipe is characterized by two distinguished zones. One is the inviscid core and the other is the thin boundary layer [10]. Through the first bend of the S-duct diffuser, an azimuthal pressure gradient appears as a result of the centrifugal force proportional to $\rho u^2/R$. This pressure gradient balances the centrifugal force that is generated due to turning of the flow. Hence, higher pressure is seen at the outer region of the bend than the inner region. Due to this pressure gradient secondary flows are created where the slower boundary layer is moving towards inside turn and the faster inviscid core is moving outward. As the flow turns over the bend, the pressure difference increases, and the fluid begins to move around the circumference of the duct. The boundary layer grows and slows down, eventually the azimuthal pressure gradient increases enough that the secondary flow lifts off and a pair of counter-rotating vortices form along the inner surface of the bend. At that point, the inviscid flow with high momentum dominates the outer part of the cross-section area while disturbed low momentum flow stays at inner part. Hence, low total pressure zone appears at the inside of the first bend ([4], [11]).

Some of the distortion that described might supposed to be reversed through the second turn by the same phenomena. However, after the first turn completed much of the low momentum fluid is located at the outside of the second bend. Thus, the strong pressure gradient that supposed to drive flow back does not occur. As a result, secondary flows are formed because of the bends and they lead to large flow distortion at AIP ([4]-[7], [9]) (Figure 2.2).

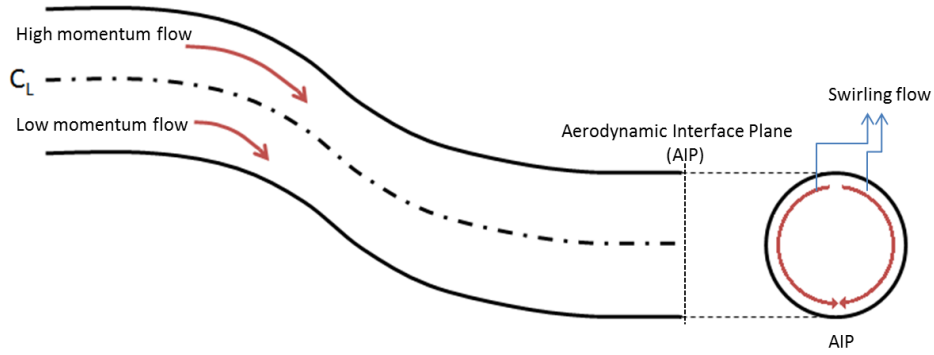


Figure 2.2: Effect of Centrifugal Forces [4]

2.2. Effects of Inlet Performance on Engine

As mentioned earlier, inlet flow structure has direct influence on engine thrust since it depends on the pressure loss through the inlet. Also, uniformity of the flow at the compressor face is critical in order to the compressor and the engine work stable. Therefore, distortion of the flow from uniform flow structure at the aerodynamic interface plane is expected to be as minimum as possible.

In fact, there is always some level of flow distortion at the AIP. However, as long as the intensity and the extension of this distortion are below some critical level it does not affect the engine operation. Although, two types of distortion can be defined as radial and circumferential; radial distortion does not affect the engine stability critically and it is usually neglected. Thus, designers are mostly interested in circumferential distortion ([6], [9], [12]). Circumferential distortion has a direct impact on engine compressor operation, as demonstrated in Figure 2.3.

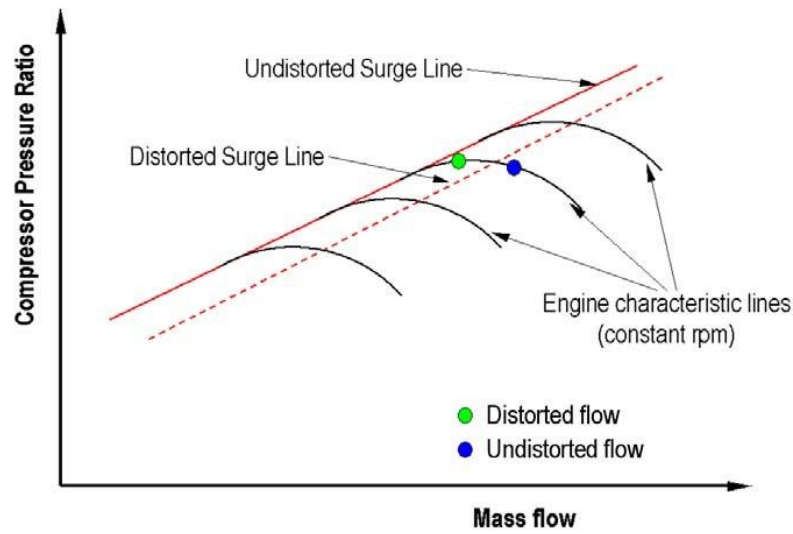


Figure 2.3: Representative Compressor Map [4]

There is always some variation in total pressure, which is related to distortion, at AIP. Because of circumferential distortion, as the compressor blades rotate the work they produce varies. They do more work at low-pressure (distorted) regions to achieve required output pressure. As a result, rotating stall can be triggered and even the compressor may end up with surge. These distorted regions are seen at the compressor maps closer to the surge line than normal operating point as in the Figure 2.3. Thus, distortion can be said to reduce the real surge margin ([5], [7]).

Flow swirl can also cause similar issues by changing the local angle of attack of individual compressor blades. It aggravates the effect of total-pressure distortion on the stability of the engines and led to surging of the engines when the swirl was contra rotational to the direction of rotation of the fan rotor blades ([6], [9]).

As previously mentioned pressure recovery drop and distortion degrade engine performance and also put the flight at risk. Considering the relation of pressure recovery with thrust, it is clear that specific thrust decreases and specific fuel consumption increases with reduced pressure recovery. Moreover, surge margin decreases for higher distortion value ([6], [13], [14]).

2.3. Inlets at Incidence

Operation of an aircraft is limited by the strength of the aircraft structure. The attainable flight conditions that an aircraft can operate safely is called flight envelope. This envelope's boundaries are formed of airspeed and load factors as “g” values and they show maneuvering capabilities of the aircraft. This envelope can then be translated into domain of incidence and yaw angles. Two such domains for a typical aircraft, one for subsonic-transonic speeds and one for supersonic speeds, as given by Hawkins [15] are illustrated in Figure 2.4.

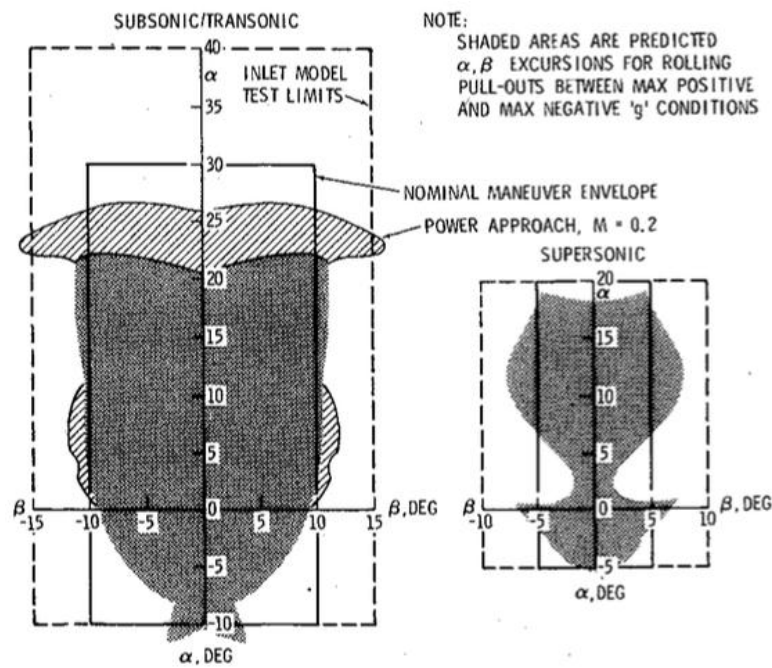


Figure 2.4: Maneuver Envelope of YF16 Aircraft at Subsonic and Supersonic Speeds [15]

Aircraft incidence may influence critically the engine performance at any flight regime. When there is an incidence, the flow at the entrance of the inlet would not be uniform and the inlet behavior is dominated by state of flow around the entry lip. Lip separation, flow asymmetry, and stagnation position variation (Figure 2.5) occur as a result of incidence and they affect the internal flow characteristics [2].



Figure 2.5: S-duct Flow Separation and Lip Separation [2]

2.4. Literature Study

Previous experimental and computational studies have been conducted to determine the characteristics of the fluid motion within S-duct diffusers. In order to provide common geometries to study this flow, mathematically defined duct shapes have been developed ([16], [17]). In the accessible literature, reviewed studies similar to the present study from the viewpoint of objectives are discussed in this section. Attention will be drawn to both experimental investigations and computational studies. The flow in S-duct air inlets is subject to two main phenomena, which cause the loss of performance and distortion at the compressor face: boundary layer separation and secondary flows. Several studies have focused on understanding the generation of those phenomena, both from a theoretical and experimental point of view.

Wellborn et al. [7] have experimentally investigated compressible flow through a serpentine inlet at $M=0.6$ and $Re=2.6 \times 10^6$. The flow has shown symmetric behavior about the geometrical symmetry plane. Streamwise flow separations regions are seen after the bends of the duct. Secondary flows are seen as a result of the duct curvature and these secondary flows turned into a pair of counter-rotating vortices at the AIP. These vortices convected the low momentum fluid of the boundary layer towards the center of the duct.

Harloff et al. [18] numerically investigated compressible flow within a diffusing S-duct and a circular-to-rectangular transition duct. They used PARC3D CFD code to solve 3D RANS equations and Baldwin-Lomax and $k-\epsilon$ turbulence models. Total and surface static pressure field for transition duct

predicted well. However, turbulence modeling needed to be enhanced to predict strong cross-flow and separated boundary layer. S-duct analyses were agreed with experiments, but both turbulence models underpredicted the length and angular extend of the boundary layer separation. More advanced turbulence models were also required to compute strong cross flow and separated boundary layer.

In a similar study, Harloff et al. [19] found that using the same turbulence models transverse flow patterns were predicted greater than experimental transverse velocities in the region of the counter-rotating vortices and less than in the core flow region.

In a numerical study, Wellborn et al. ([20], [21]) examined compressible flow structure in a diffusing S-duct. Computations are conducted with PARC3D code and Baldwin-Lomax and $k-\epsilon$ turbulence models were used for solutions. Strong cross flow total pressure nonuniformity and separation regions were simulated. As the separated region blocking the cross section of the flow, increased velocities were observed at the rest of the cross-section area. Increased velocity resulted in larger shear stress levels and larger total pressure losses. The reattachment point has found to be at a further position than experimentally obtained. Moreover, the predicted cross flow transferred less amount of low momentum flow than the experiment. The authors declared that in order to overcome this issue more advanced turbulence models are required.

Tindell [22] computed the flow mechanisms in an S-duct diffuser using a three-dimensional Navier-Stokes code, ARC3D. He also conducted experiments and took measurements of static and total pressures throughout the diffuser and across the exit plane. Lower surface separation zone is found to be primary driver of swirling flow that significantly affects AIP total pressure profile. Calculated duct exit total-pressure levels near the inboard wall conflicted with the experiments. Analyses accurately predicted the total pressure increases measured along the lower surface. Nondimensional performance parameters that obtained by integrating the calculated total pressure field at the AIP were predicted well.

Breiar et al. [8] researched the structure of a flow separation within a UCAV inlet during cruise. He used NASA CNS code for numerical simulations. Numerical analyses were conducted with full scale geometry whereas experiments were performed with $1/6^{\text{th}}$ scale of the inlet. Mach number were set to cruise Mach number for both analyses and experiments, while Re were different because of the scaling. In experiments, a bellmouth is used to eliminate inlet separations related to maneuvering. In addition to wall static pressures and AIP total pressure measurements, flow visualization is performed. Analyses were conducted at about 470,000 nodes and turbulence is modeled with k- ω model. The same separation zone is preserved while Mach number is increasing. Pressure recovery had seen to be reduced with mass flow rate above design conditions. This was contributed to the Mach number variation, instead of Reynolds number, as a result of increased adverse pressure gradient and boundary layer thickness. The study demonstrated that stronger adverse pressure gradients cause stronger separations, which should therefore lead to reduced pressure recovery and increased inlet unsteadiness.

Kirk et al. ([23], [24]) conducted a numerical and experimental study to reveal the separation points and the strong secondary flow phenomena within the S-duct inlet. Fluent[®] commercial code and UNS3D in-house code were used to solve RANS equations. The turbulence effects were modeled by using the shear-stress transport k- ω model. Experiments were performed in an open circuit, low-speed wind tunnel at the duct entrance conditions of $M=0.17$, and $Re=1.02 \times 10^6$. AIP is traced with a 7-hole probe and wall static pressures are measured through the duct symmetry plane at upper and lower surfaces. In additions surface visualization experiments were conducted. Qualitatively, there was good agreement between the CFD results of both codes and the experimental data. Counter rotating vortices were detected in both experiments and analyses. UNS3D overpredicted the locations of the first separations, while the area-averaged pressure loss coefficient was 5% higher than in the experiment.

Fiola and Agarwal ([25], [26]) conducted the numerical simulations of compressible flow inside an S-duct using Fluent commercial code. The three-dimensional RANS equations were solved on a structured mesh with the Spalart–Allmaras (SA), k - ϵ , k - ω SST, and Transition SST turbulence models. A second-order accurate, steady, density-based solver was employed. The computed results of the flow field and pressure recovery were agreed with the experimental data. However, some discrepancies were observed and further improvements in the computational model were needed. It was found that k - ω SST turbulence model gives best agreement with the experimental data in predicting the pressure distribution along the duct at various angular locations, the separated flow region (both the separation and reattachment points), and the secondary flow.

Gerolymos et al. [12] studied the capability of RANS analyses using seven-equation Reynolds-stress model for flows in aircraft-engine inlet double-S-duct configurations. The inlet had been tested experimentally at ONERA and these experimental data were used for comparison. Analyses were conducted using the GV RSM, and WNF-LSS RSM approaches and also baseline LS the numerical results are compared with that data and also k - ϵ model. The results indicated that the GV RSM predicts with reasonable accuracy this difficult test

Hawkins [15] summarized the design and development process of YF-16 (prototype of F16) inlet and performance characteristics of the inlet throughout the flight and maneuver envelope of the airplane. Pressure recovery, distortion, turbulence, inlet stability, and spillage drag was analyzed at critical angle of attack, side slip angles and Mach numbers. Level flight pressure recovery is maintained up to 30° angle of attack for subsonic flight; while increase in it was seen with angle of attack occurs at supersonic speeds. The study revealed with the help of inlet flow controllers that the distortion and stability for the flow was not an issue for the engine.

Menzies [27] simulated the experimental flow cases in M2129 intake that is conducted by Royal Aircraft Establishment. A validation study was undertaken on the steady through-flow problem. RANS simulations were performed with

SA, $k-\omega$ and SST turbulence models. Afterwards, incidence angle conditions were analyzed.

Aslan et al. [28] investigated experimentally aerodynamic characteristics of an S-duct inlet designed for a micro turbojet engine powered aircraft at various flow rates. Measurements have shown that stream wise flow separation is occurred within the duct. Total pressure loss is seen as a result of the flow structure.

CHAPTER 3

EXPERIMENTAL SETUP AND RESULTS

Aerodynamic performance of the S-duct air inlet that was designed for a micro turbojet engine powered aircraft is studied experimentally. In this chapter experimental setup is explained. During the tests inlet wall and aerodynamic interface plane (AIP) pressure distribution are investigated. For 3 different mass flow rates wall pressure measurements and exit pressure profiles are presented.

3.1. Test Section

An experimental data set from tests with an S-duct diffuser, designed for a micro turbojet engine powered aircraft was used for the assessment of the numerical simulations. The experiments related to the present study were conducted in a subsonic blow down wind tunnel that is located at TEI. This wind tunnel is an open-circuit, low-speed facility [28].

Test setup is configured such that the outlet of the diffuser is open to the atmosphere. The other side of the serpentine diffuser is mounted impermeable by a flange to the wind tunnel settling chamber. The schematic view of the test section is shown in Figure 3.1.

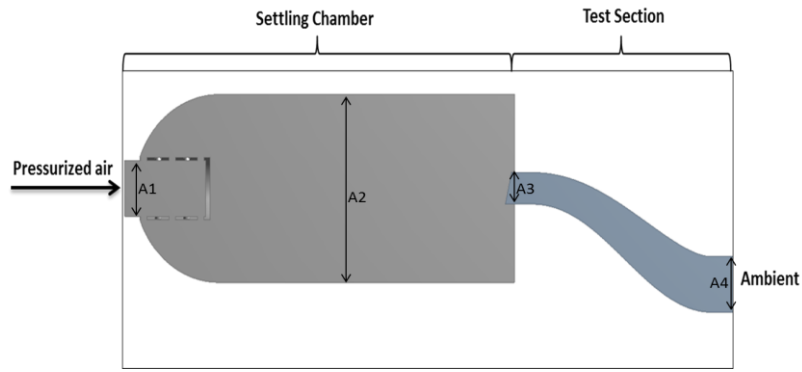


Figure 3.1: Schematic View of the Test Setup

From A1 to A4 define the cross section areas through the wind tunnel and the S-duct inlet. The cross section area ratios are tabulated in Table 3.1.

Table 3.1: Geometrical Parameters Defining the Test Section

Quantity	Value
$A1/A2$	0.088
$A2/A3$	13.40
$A3/A4$	0.86

The wind tunnel pressurized air is supplied by large industrial compressors, which can provide up to 10 bars of pressure inlet conditions. There is a settling chamber before the S-duct to stabilize inlet air conditions. Using an electrically actuated valve mass flow rate is controlled. While inlet and outlet pressures are steady, valve throat area sets the mass flow rate.

The wind tunnel is provided with a static pressure sensor and a temperature sensor at the plenum. It is known that at the plenum air is still, thus, plenum static pressure can also be used as plenum total pressure.

3.2. S-duct Inlet

The studied S-duct inlet is designed for flight speeds around Mach number 0.6. It is manufactured using rapid prototyping and there is some surface roughness to be considered. Schematic view of the S-duct inlet is demonstrated in Figure 3.2. Parameters, which defining the S-duct geometry, are listed in Table 3.2.

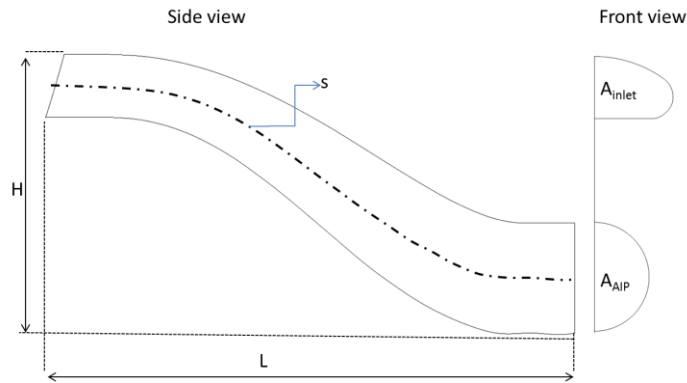


Figure 3.2: Schematic View of the S-duct Inlet

Table 3.2: Geometrical Parameters Defining the S-duct Model

Quantity	Value	Description
$A_{\text{inlet}}/A_{\text{AIP}}$	0.86	S-duct diffusion ratio
H/L	0.53	S-duct height to length ratio
s/L	1.08	S-duct centerline to length ratio

3.3. Instrumentation

In order to see wall static pressure distribution, 13 static pressure taps on top of the symmetry plane and 13 static pressure taps under bottom the symmetry plane were drilled as in the Figure 3.3. Positions of these taps were suggested as a result of preliminary CFD calculations and they are not equally distributed.

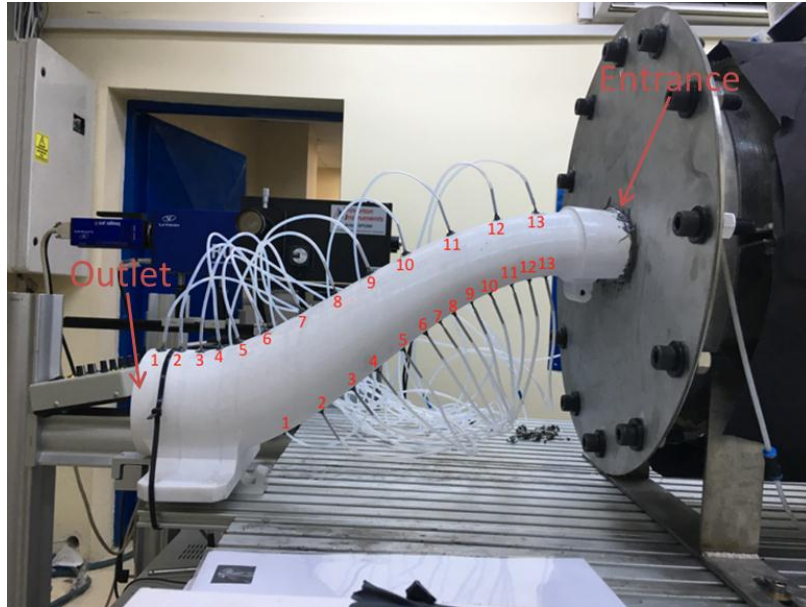


Figure 3.3: Instrumentation and Test Section

S-duct diffuser outlet pressure distribution was measured using a Pitot-static measurement probe of 1.6mm of diameter. An automatically controlled 2D linear traverse system was used to move the probe across the diffuser exit area (Figure 3.4). Because of the symmetry, only right hand side of the exit area was traversed. Right hand side of the exit plane was divided into equal areas and measurements were taken from the centroids of these equal areas (Figure 3.5).

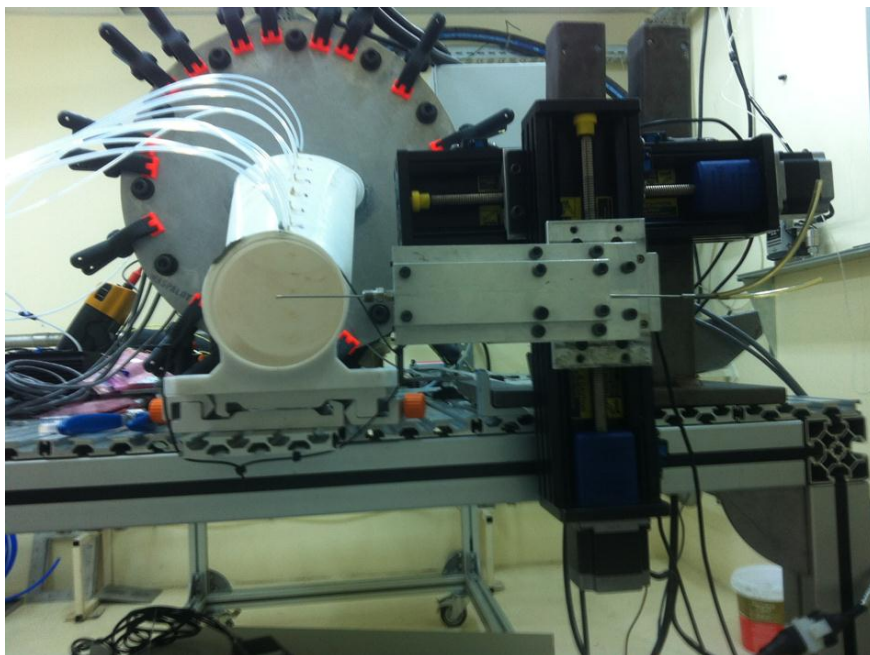


Figure 3.4: 2D Linear Traverse System Configuration

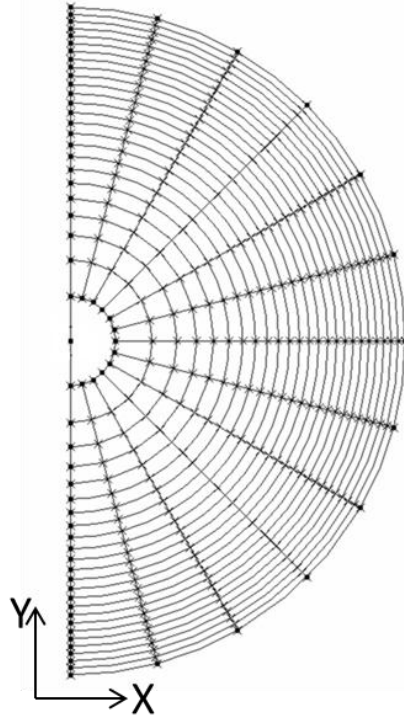


Figure 3.5: AIP Measurement Locations

Moreover, plenum chamber and atmospheric pressures were measured as well. Atmospheric temperature was measured using a K-type thermocouple. Mass flow rate was obtained using a thermal flow meter, which is located previous to plenum chamber. Atmospheric pressure is measured with a capacitive absolute pressure transducer, while gauge pressures are measured with capacitive differential pressure transducers

Pressure sensors accuracy was $\pm 0.04\%$ of measurement, while mass flow rate measurement was $\pm 0.1\%$ accurate. Instrument properties are listed in Table 3. The data was recorded using NI cDAQ data acquisition system at a sampling rate of 100Hz.

Table 3.3: Instrument Properties

Product	Range	Uncertainty
Pressure Sensor (for atmospheric pressure measurements)	0-2 bar	±0.04% Full Scale
Pressure Sensor (for wall static pressure measurements)	0-0.35 bar	±0.04% Full Scale
Temperature Sensor	-200-1250°C	±0.04% Full Scale
Mass Flow Meter	0-0.3 kg/s	±0.1% Full Scale

Inlet flow control parameter was mass flow rate. Experiments were performed at three different mass flow rates as given in Table 3.4. M and Re are also listed for the given test conditions.

Table 3.4: Mass Flow Rates

Case #	1	2	3
\dot{m}/\dot{m}_{\max}	0.57	0.82	1
M	0.07	0.10	0.12
Re	140638	205094	248316

3.4. Data Reduction

All data presented in this study are in non-dimensional form. Aerodynamic results represent mean values. Pressures are presented as gauge pressure ratios (GPR), which is defined by equation (3.1).

$$GPR = \frac{p - P_{atm}}{P_{\infty} - P_{atm}} \quad (3.1)$$

Here, $p - P_{atm}$ is the gauge pressure at the measurement point, $P_{\infty} - P_{atm}$ is the gauge pressure at the settling chamber and P_{atm} is the free atmospheric pressure.

Moreover, non-dimensional parameters that quantify the output of the engine inlet are defined in literature. These inlet performance parameters, which are pressure recovery and distortion parameter, are explained below.

3.4.1. Pressure Recovery

The gas turbine engine accepts air into the compressor or fan face at a Mach number around 0.4 or 0.5. Hence, above this, the inlet operates as a diffuser such as decelerating the flow and increasing static pressure. That's why the term pressure recovery is used to define efficiency of the inlet. As this definition is irrelevant at other Mach values, total pressure ratio is used instead of static pressure ratio to define pressure recovery. Since total pressure falls because of losses coming from boundary layer, shock waves and separation; that definition let the flow to be analyzed by these flow phenomena.

Then, pressure recovery (PR) is most commonly defined as in equation (3.2):

$$PR = \frac{P_{AIP}}{P_{\infty}} \quad (3.2)$$

where, P_{AIP} is the mean total pressure at the engine face. However, as Mach number goes to zero that definition goes to unity and unable to determine whether the losses are small or great. Therefore, an alternative description is the incompressible flow ratio can be used for free stream velocities under 0.3 M, as shown in equation (3.3) [1]:

$$\eta_{\sigma_i} = \frac{P_{AIP} - p_{atm}}{P_{\infty} - p_{atm}} \quad (3.3)$$

3.4.2. Compatibility Features

In order to quantify the quality of the flow, numerical parameters are also required. Different aircraft engine manufacturers found their own distortion

descriptors for that purpose. One of the most widely used and easiest to calculate descriptor is that developed by Rolls Royce PLC for steady circumferential distortion is defined in equation (3.4) [1].

$$DC(\theta) = \frac{P_{AIP} - P_{\theta}}{q_{AIP}} \quad (3.4)$$

The $DC(\theta)$ engine face distortion descriptor is a measure of the difference between the engine face or AIP average total pressure (P_{AIP}) and the lowest average total pressure in any sector defined by a critical angle of θ° (P_{θ}), divided by the average dynamic pressure at the engine (q_{AIP}) face (Figure 3.6).

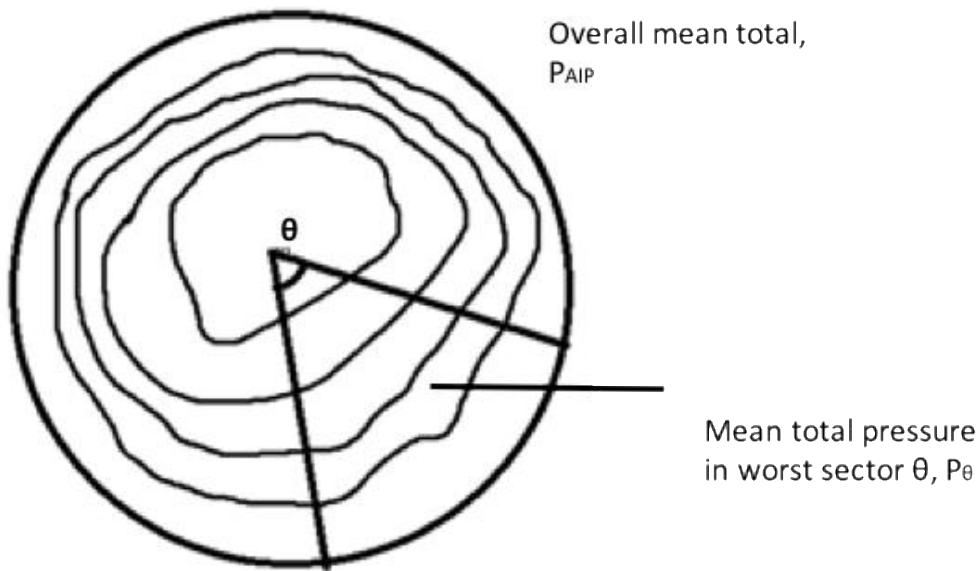


Figure 3.6: Illustration of Total Pressure Contours and θ Sector for Definition of Distortion Coefficient [6]

All of the area searched with sectors of θ as seen in Figure 3.6 [5]. Then, the lowest average sector is inserted to the equation. The choice of the sector angle value must be significant enough that the compressor blades feel the impact of distortion, thus flow reaches steady state [4]. A commonly used coefficient is $DC(60)$; others, which are also used, are $DC(90)$ and $DC(120)$. 60° will be used in this study, as it is the angle most commonly used in literature. Thus, total pressure steady-state distortion descriptor will be $DC(60)$ [7].

3.5. Experimental Results

GPR variation through the duct is shown in Figure 3.7 and Figure 3.8.

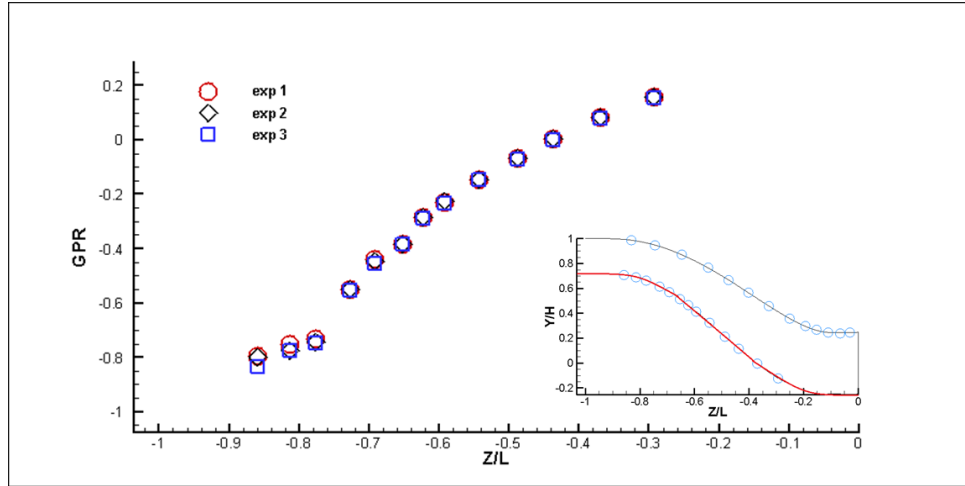


Figure 3.7: Top Wall GPR through the Duct

Low pressure is seen at the entrance because of the lip separation and it increases through the reattachment zone. Then, GPR decreases again as a result of separation due to second turn.

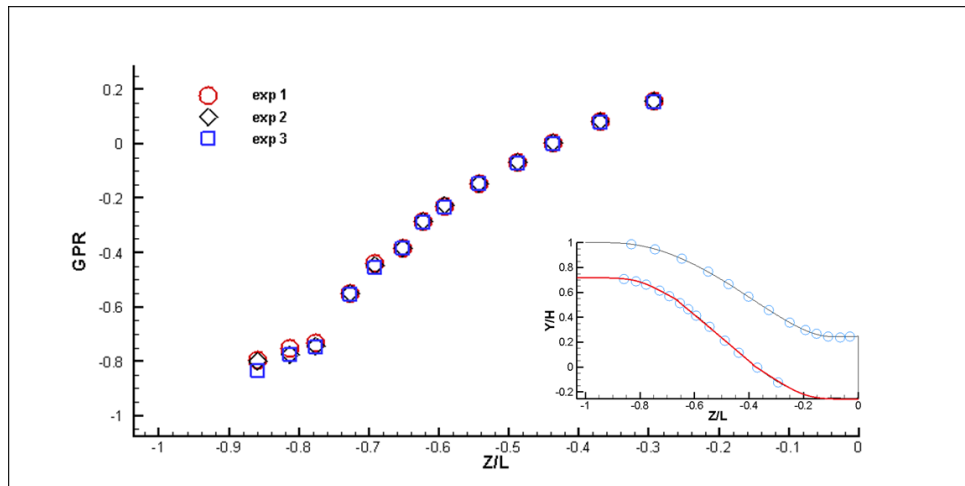


Figure 3.8: Bottom Wall GPR through the Duct

Remarkably low GPR value is seen at the bottom of the duct through the first bend. This is caused by the separation due to turning of the flow. Afterward GPR increases gradually through the reattachment point at the second bend.

Pointwise ($\eta_{\sigma,i}$) contours are demonstrated in Figure 3.9.

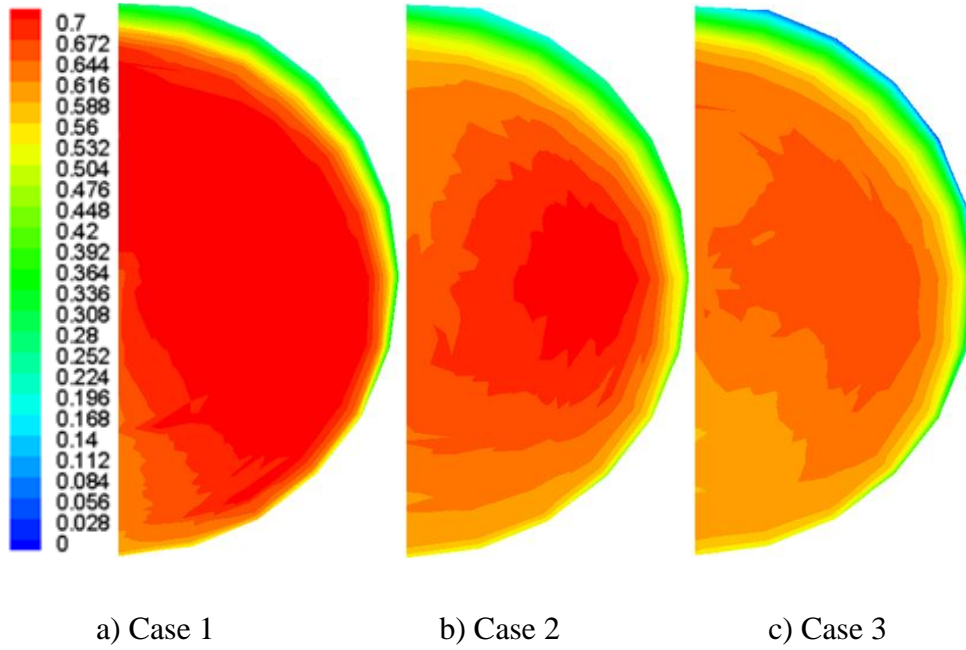


Figure 3.9: ($\eta_{\sigma,i}$) Contours at AIP

It is seen that circumferential lowest pressure distribution is seen at the lower part of the outlet. It is expected as a result of swirling flow because of bends of the diffuser. Furthermore, pressure deficiency is seen at the top region as well. Pressure drop at this region is expected because of the separation due to second turn. Table 3.5 shows the performance parameters for the three test cases.

Table 3.5: Performance Parameters

Case #	1	2	3
\dot{m}/\dot{m}_{\max}	0.57	0.82	1
PR	0.9986	0.9970	0.9954
$\eta_{\sigma,i}$	0.670	0.615	0.583
DC60	0.050	0.079	0.045

It is observed that as the mass flow rate increases, total pressure loss of the flow also increases. However, the magnitude of the pressure loss is below 1%. Although, the amount of pressure loss seems to be small, it should be kept in mind the velocities tested in this study is much lower than the real flight speeds and in real flight conditions PR can reach critical values for engine operation. Since the experimental velocities are low, incompressible flow ratio (η_{σ_i}) will be given more importance than PR from now on as described in Chapter 2. DC60 parameter, which shows the circumferential distortion characteristics, was also calculated. However, DC60 does not follow a trend with mass flow rate variation considering the given test conditions.

Using wall static pressure measurements separation regions were caught through the first and second bends of the S-duct diffuser. Flow separation is one of the main contributors of pressure loss with secondary flows. Total pressure loss is seen to increase with increasing mass flow rate. Although the measured pressure loss is small for the test conditions, increasing trend can be resulted in large numbers at flight conditions.

Main parameters that define an engine inlet performance are investigated. Some of the flow characteristics are obtained for the given S-duct for three different test conditions. While, the capability of the test facility does not allow investigating higher mass flow rates; low mass flow rate test results can be used for numerical simulation validation, and other flight conditions can be investigated also by simulation.

CHAPTER 4

VALIDATION STUDY FOR NUMERICAL SIMULATIONS

A numerical investigation of the flow field in a short, diffusing S-duct inlet was conducted in comparison with an experimental setup available in literature. The objective of this study is to investigate aerodynamic characteristics of a serpentine inlet at attached entrance conditions numerically and to verify the numerical tools using the experimental data set taken from literature ([16], [29]). Flow characteristics such as separation, secondary flows, and swirl are investigated to find out the source of distortions and pressure loss at aerodynamics interface plane. Grid refinement study is conducted also with this validation case. Then, performance of various turbulence models for the given test case is evaluated.

4.1. Case Definition

An experimental data set from tests with the RAE M2129 diffuser model provided by QinetiQ was used for the assessment of the numerical simulations ([16], [29]). This model was designed by the Royal Aircraft Establishment (a predecessor of QinetiQ) for academical purposes. The experiments related to the present study were conducted at RAE Bedford (UK) in the 13ft x 9ft wind tunnel. This wind tunnel is a closed circuit, atmospheric pressure, and low-speed facility. An ejector mounted at the rear of the inlet was used to provide the pressure difference between the inlet and exit planes of the inlet model that driving the flow. Experiments were conducted at freestream Mach number of 0.21. A bellmouth is mounted to the entrance of the S-duct diffuser to prevent

lip separation. Hence, this study simulates uniform inlet conditions such as seen in cruise flight. The data include mean quantities on the duct walls and at the engine face.

4.2. M2129 Diffuser Geometry

M2129 S-duct diffuser geometry is shown in Figure 4.1. The area ratio between the engine face section and throat section is equal to $A_{AIP}/A_{throat} = 1.40$, the throat diameter being equal to 128 mm. The offset of the model (H) resulting from the centerline curvature is $1.065 D_{throat}$ and the length of the duct (L) is $4.668 D_{throat}$.

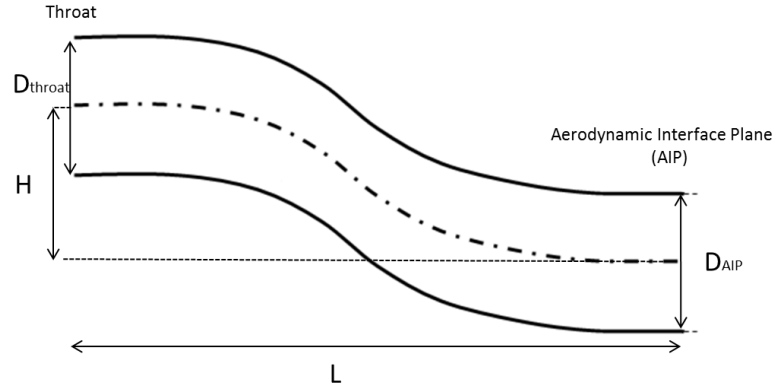


Figure 4.1: M2129 Diffuser Geometry

For the M2129 S-duct configuration, the centerline and the diameter are defined by equations (4.1 – 4.3)

$$y = 0.0 \quad (4.1)$$

$$z = -0.15L \left(1.0 - \cos\left(\frac{\pi x}{L}\right) \right) \quad (4.2)$$

$$D = D_{throat} + (D_{AIP} - D_{throat}) \left(3.0 \left(1.0 - \frac{x}{L} \right)^4 - 4.0 \left(1.0 - \frac{x}{L} \right)^3 + 1.0 \right) \quad (4.3)$$

where x belongs to the interval $[0, L]$ and L is the duct length. D_{throat} is the throat diameter and D_{AIP} is the diameter at the engine face location x_{AIP} . This gives an offset in the z -direction of $1.065 D_{throat}$. The duct has an upstream lip and parallel extension as well as a downstream parallel extension that includes

the engine face and the outflow boundary domain. All geometrical parameters are given in Table 4.1.

Table 4.1: Geometrical Parameters Defining the RAE M2129 S-duct Diffuser Model [29]

Quantity	Value	Description
D_{throat}	0.1288 m	Throat diameter
D_c	0.1440 m	Highlight (entry) diameter, capture area
D_{AIP}	0.1524 m	Diameter at the engine face
X_{AIP}	0.4839 m	Engine face position
L	0.4572 m	Duct length

4.3. Numerical Approach

In order to simulate the flow structure in the S-duct diffuser, defined control volume is discretized and conservation laws of the mass (continuity), momentum and energy are applied to each discrete volume. Each conservation equation is solved at every finite volume iteratively until the predefined convergence criteria in flow parameters is achieved.

The continuity and momentum equations governing the fluid system are given in equations (4.4 – 4.7) [30]:

Continuity equation:

$$\frac{\partial \rho}{\partial t} + \nabla \cdot (\rho \vec{V}) = 0 \quad (4.4)$$

where \vec{V} is velocity, ρ is density.

Momentum equations:

$$\text{x-component : } \frac{\partial(\rho u)}{\partial t} + \nabla \cdot (\rho u \vec{V}) = -\frac{\partial p}{\partial x} + \frac{\partial \tau_{xx}}{\partial x} + \frac{\partial \tau_{yx}}{\partial y} + \frac{\partial \tau_{zx}}{\partial z} + \rho f_x \quad (4.5)$$

$$\text{y-component : } \frac{\partial(\rho v)}{\partial t} + \nabla \cdot (\rho v \vec{V}) = -\frac{\partial p}{\partial y} + \frac{\partial \tau_{xy}}{\partial x} + \frac{\partial \tau_{yy}}{\partial y} + \frac{\partial \tau_{zy}}{\partial z} + \rho f_y \quad (4.6)$$

$$\text{z-component : } \frac{\partial(\rho w)}{\partial t} + \nabla \cdot (\rho w \vec{V}) = -\frac{\partial p}{\partial z} + \frac{\partial \tau_{xz}}{\partial x} + \frac{\partial \tau_{yz}}{\partial y} + \frac{\partial \tau_{zz}}{\partial z} + \rho f_z \quad (4.7)$$

where u, v, w are the x, y, z components of the velocity respectively; p is pressure, τ is shear stress, \vec{f} is body force per unit mass.

The energy equation is given in equation (4.8)

$$\begin{aligned} \frac{\partial}{\partial t} \left[\rho \left(e + \frac{V^2}{2} \right) \right] + \nabla \cdot \left[\rho \left(e + \frac{V^2}{2} \vec{V} \right) \right] = \rho \dot{q} + \frac{\partial}{\partial x} \left(k \frac{\partial T}{\partial x} \right) + \frac{\partial}{\partial y} \left(k \frac{\partial T}{\partial y} \right) + \\ \frac{\partial}{\partial z} \left(k \frac{\partial T}{\partial z} \right) - \frac{\partial(u p)}{\partial x} - \frac{\partial(v p)}{\partial y} - \frac{\partial(w p)}{\partial z} + \frac{\partial(u \tau_{xx})}{\partial x} + \frac{\partial(u \tau_{yx})}{\partial y} + \frac{\partial(u \tau_{zx})}{\partial z} + \frac{\partial(v \tau_{xy})}{\partial x} + \\ \frac{\partial(v \tau_{yy})}{\partial y} + \frac{\partial(v \tau_{zy})}{\partial z} + \frac{\partial(w \tau_{xz})}{\partial x} + \frac{\partial(w \tau_{yz})}{\partial y} + \frac{\partial(w \tau_{zz})}{\partial z} + \rho \vec{f} \cdot \vec{V} \end{aligned} \quad (4.8)$$

where e is internal energy per unit mass, \dot{q} is the rate of volumetric heat addition per unit mass, T is temperature, k is the thermal conductivity.

4.4. Grid Generation

Since of the geometry is symmetrical, only one half portion of the inlet is considered for the finite volume computations. In order to simulate inlet conditions of the duct, a hemispherical large domain is added to the flow model. The unstructured tetrahedral cells with prism layers at the duct walls are preferred (Figure 4.2). Mesh dependency of the solution is surveyed using coarse, medium and fine grid structures. 24 layers with 1.2 growth rate is used for boundary grid mesh. 0.01 mm of first layer thickness is used for the fine grid structure.

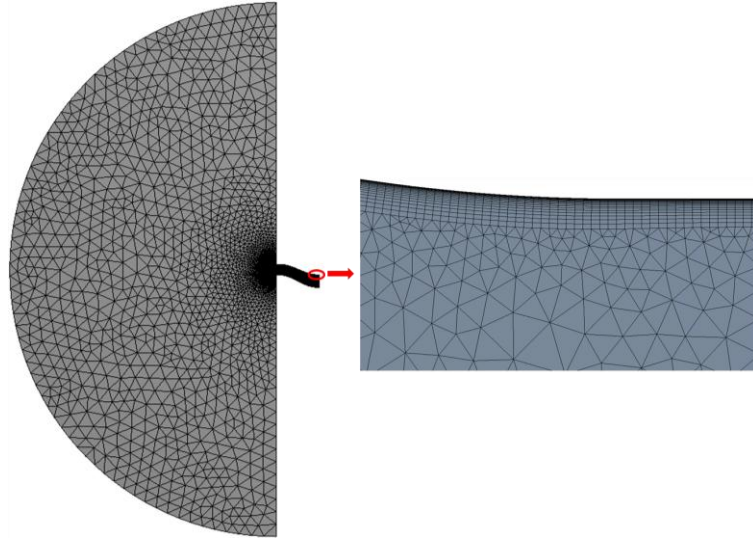


Figure 4.2: Mesh Structure

4.5. Boundary Conditions

The boundary conditions for the test case ([16], [29]) that was investigated are shown in Table 4.2.

Table 4.2: Boundary Conditions

Quantity	Value
M	0.207
α	0°
β	0°
p_{∞}	100018.8 N/m ²
T_{∞}	280.2 K
ρ_{∞}	1.244 kg/m ³
Re	4932254
\dot{m}	2.873 kg/s

Pressure-far field boundary condition is set to spherical surface of this domain with 0.207 Mach and 100018.8 Pa static pressure value. The temperature at these conditions is 280.2 K. The free outlet condition (pressure outlet) is located on the flat surface of the hemispherical domain with static pressure and temperature conditions same as the inlet boundary. The duct exit is also set to pressure outlet. However, the pressure value is established after an iterative process. These iterations are continued until the predicted mass flow rate and the experimental one are matched. At the duct walls, no slip condition is applied and the cut surface of the numerical domain is treated as symmetry boundary condition.

4.6. CFD Flow Solver

All the 3D numerical simulations are performed using commercially available general purpose CFD code ANSYS Fluent [31]. Pressure-Based solver has been used for turbulent investigations. For the pressure-velocity coupling, SIMPLE algorithm is selected. As setting the spatial discretization, all the variables except pressure, second order upwind scheme is used and for the pressure, PRESTO! scheme is preferred. During the computations the air is considered as ideal gas to model compressibility effect.

4.7. Turbulence Modeling

One of the aims of this work is to reveal the capabilities various turbulence closures in modeling complex internal flows. The flow is challenging with complex secondary flows and strong pressure gradients, hence, turbulence modeling is important.

In order to describe turbulent flows Reynolds [32] proposed a statistical approach. The idea is to decompose the instantaneous quantities that seen in Navier-Stokes equations into time-averaged and fluctuating quantities. That's why they are called as Reynolds-averaged Navier–Stokes (RANS) equations. However, the fluctuation terms are uncorrelated with the mean flow values and additional nonlinear terms appear in the equations because of them. Because of

the nonlinearity it is almost impossible to solve these equations analytically. Therefore, these nonlinear terms are supposed to be modeled using other equations for closure of RANS equations.

Various number of turbulence models have been developed to reveal the turbulent flow structure. However, none of them is considered as the best or worst for all cases. Each of them gives appropriate results for some flow structure and fails beyond. In this study turbulence flow is modeled with three different RANS turbulence models namely: one equation model Spalart-Almaras (SA) and two equation models Realizable k- ϵ (RKE) and k- ω -SST. Performances of these models are compared regarding to the results.

4.8. Results

In the numerical analyses, three different grid resolutions are tested with Realizable-k- ϵ turbulence model that is selected according to its certain mathematical background and ability to give satisfactory results for many engineering fluid mechanics problems. Mesh dependency of the solution is surveyed using coarse, medium and fine grid structures. 24 layers with 1.2 growth rate is used for boundary grid mesh. 0.01 mm of first layer thickness is used for the fine grid structure. Variation of y^+ values with respect to mesh size is controlled and shown in Table 4.3.

Table 4.3: Mesh Size and y^+ Relation

Mesh size	y^+
3.1M	6-7
7.5M	5
15.5M	1-2

Results of the calculations for different mesh sizes were similar to each other. However, computations are continued with the fine mesh structure, 15.5M cells. This mesh size is chosen because of the smallest y^+ values are seen at this condition. Hence, it is more reliable for near wall solutions.

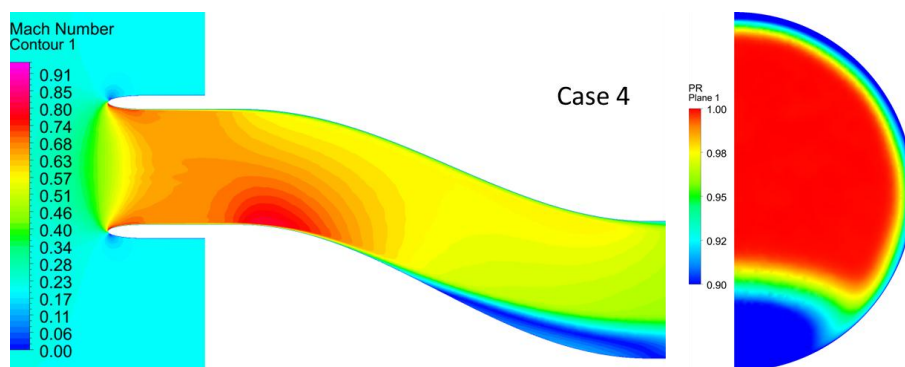
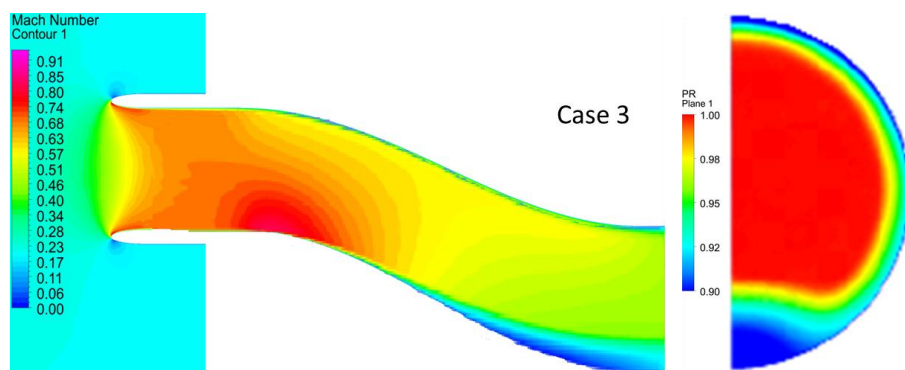
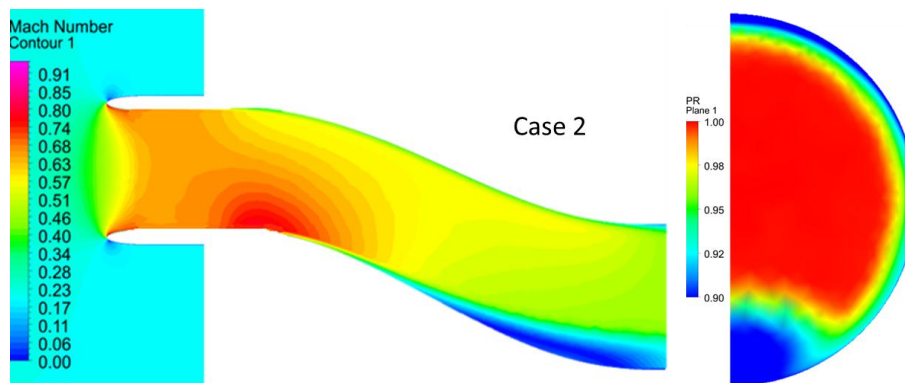
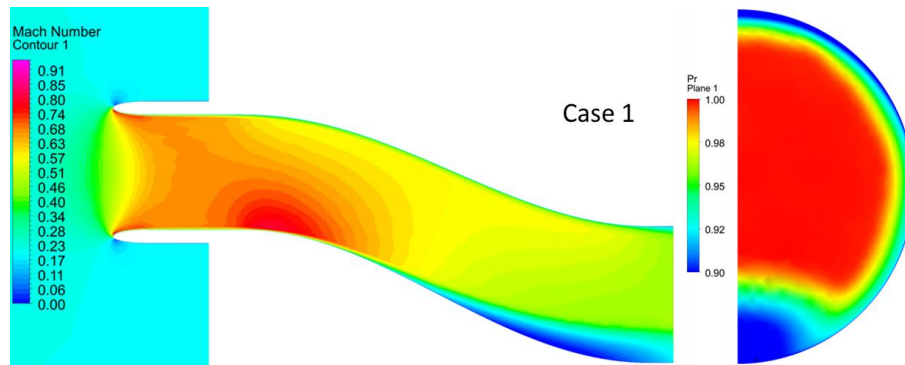
Following the grid size study, other turbulence models are tested with selected grid. Results of grid resolution study with respect to turbulence model and y^+ values are listed at Table 4.4.

Table 4.4: Analyses Conditions

Case	Turbulence model	Mesh size	y^+
1	RKE-EWF	3.1M	6-7
2	RKE-EWF	7.5M	5
3	RKE-EWF	15.5M	1-2
4	SST	15.5M	1-2
5	SA	15.5M	1-2

Here RKE-EWF stands for Realizable-k- ϵ with enhanced wall function, SST stands for Menter's Shear Stress Transport and SA stands for Spalart-Allmaras turbulence models.

Symmetry plane Mach contours and outlet pressure recovery contours for the stated analysis are shown in Figure 4.3.



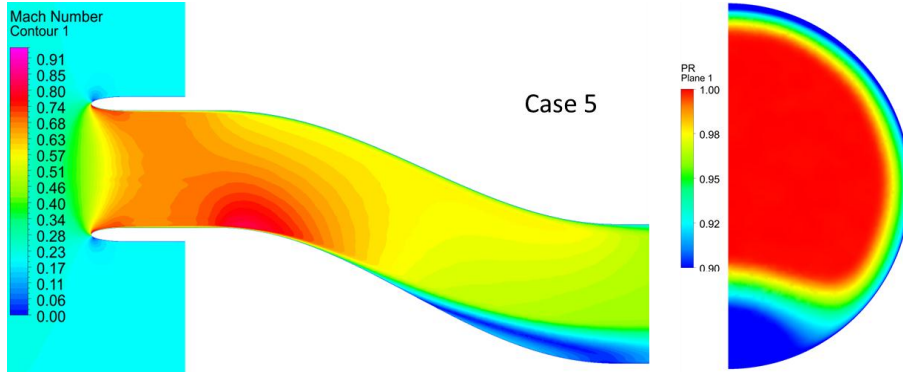


Figure 4.3: Contour Plots for Analysis (Cases 1-5)

All of the analyses show similar characteristics. At the symmetry plane highest and lowest Mach number regions and magnitudes are almost the same for all computations. However, the sizes of the regions seem to vary a little. Likewise, at the outlet plane PR contours are nearly the same.

Pressure recovery (PR) at the outlet plane obtained from the experiment is shown in Figure 4.4.

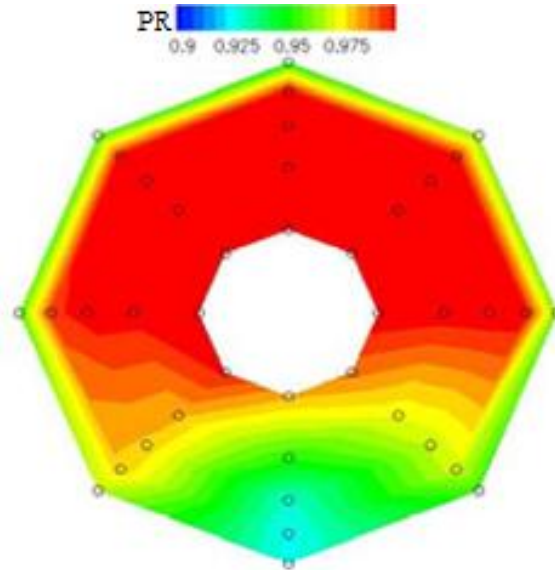


Figure 4.4: Experimental Pressure Recovery Contour at the Outlet Plane [29]

The pressure recovery contour that obtained from the experiment reveals similar distribution with the computations. However, gradient variations seem smoother at the experiment.

Computational results are tabulated in Table 4.4. They are also compared with the experimental results. PR and Mach number are calculated as the area averages at the outlet plane.

Table 4.5: Comparison of Numerical and Experimental Data

Case	PR	Mach	Mass flow
1	0.9763	0.414	2.846
2	0.9762	0.411	2.826
3	0.9772	0.420	2.887
4	0.9733	0.417	2.847
5	0.9754	0.419	2.871
Experiment	0.9798	0.395	2.873

By defining the outlet pressure iteratively, mass flow rates are obtained close to the experimental one. However, the numerically calculated Mach numbers take values higher than 0.41, it is still in a good agreement (about %3-4 deviation from experimentally calculated speed.) Anyway, the pressure recovery parameter is in range of experimental data. Even though the pressure gradients of the numerical analysis at the outlet plane look drastic with respect to experiment, area weighted averages are found very close to each other.

Flow structure in a short, diffusing S-duct inlet is numerically investigated. Computations are compared with the experimental data obtained from the study conducted at RAE facilities for numerical validation. RANS solutions have been computed with freestream Mach number fixed at 0.207 and Reynolds number based on the non-dimensional engine face diameter of 777,000.

The results were found to compare well with experiment. Spalart-Almaras turbulence model gives the most suitable results considering mass flow rate, Mach number and pressure recovery values together.

CHAPTER 5

NUMERICAL INVESTIGATION OF THE S-DUCT DIFFUSER FLOW STRUCTURE

Numerical investigation of the flow structure in an S-duct diffuser that was designed for a micro turbojet engine powered aircraft is performed. The objective of this study is to investigate aerodynamic characteristics of a serpentine inlet numerically and to survey the performance of the numerical simulations for various entrance conditions using the experimental data that was shown in Chapter 3. Mesh dependency study for the numerical analyses is carried out. Afterwards, performance of various turbulence models for the given test case is evaluated. Moreover, the effect of inlet profile on upstream flow structure is surveyed.

5.1. Case Definition

An experimental data set from tests with an S-duct diffuser, designed for a micro turbojet engine powered aircraft was used for the assessment of the numerical simulations. The experiments related to the present study were conducted in a subsonic blow out wind tunnel. This wind tunnel is an open-circuit, atmospheric pressure, low-speed facility. For details of the case see Chapter 3.

5.2. Numerical Approach

All the 3D numerical simulations are performed using commercially available general purpose CFD code ANSYS Fluent. Because of the geometrical

symmetry, only one half portion of the geometry is considered and for the finite volume computations. The hexahedral cells with prism layers at the duct walls are preferred. Mesh dependency of the solution is surveyed using base, coarse, medium and fine grid structures. 20 layers with 1.2 growth rate is used for boundary grid mesh. 0.01 mm of first layer thickness is used for the fine grid structure.

For the base solution the domain that containing both S-duct diffuser and the plenum chamber is computed. Boundary conditions are defined as mass flow inlet at the entrance of plenum chamber and the outlet pressure at the exit of S-duct diffuser. From this solution wall effect of plenum chamber at the S-duct entrance is observed. The computed velocity profile at the entrance of S-duct diffuser is recorded and used as the inlet boundary condition for the rest of the analyses. By this way, the rest of the computations are conducted for the S-duct diffuser domain only. Hence, denser grid structure can be analyzer with the available computing source.

Variation of y^+ values with respect to mesh size is controlled and the mean values all along the walls are shown in Table 5.1. Here, given number of cells are for the S-duct diffuser domain.

Table 5.1: Mesh Size and y^+ Relation

Case	Turbulence model	Mesh size	y^+
1	Realizable k- ε (RKE)	656736	18
2	Realizable k- ε (RKE)	1449600	4.28
3	Realizable k- ε (RKE)	3172820	1.45
4	Realizable k- ε (RKE)	4682400	0.35

Results of the calculations for different mesh sizes were similar to each other. However, computations are continued with the fine mesh structure, about 4.7 M cells (Figure 5.1). This mesh size is chosen because of the smallest y^+ values are seen at this condition. Hence, it is more reliable for near wall solutions.

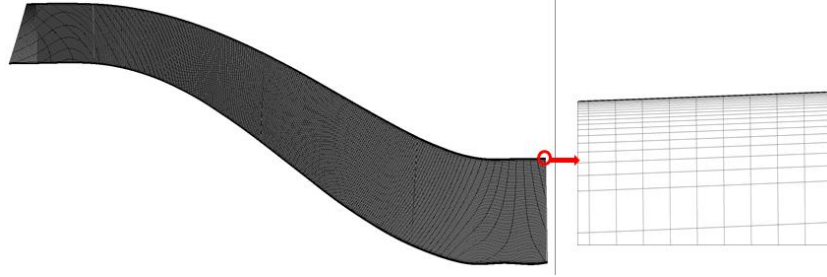


Figure 5.1: Mesh Structure

The turbulent flow field has been investigated with Pressure-Based solver. In order to capture turbulent flow characteristics, four different RANS turbulence models are used, namely: one equation model Spalart-Almaras, two equation models Realizable $k-\varepsilon$ and $k-\omega$ -SST and seven equation model Reynolds Stress Model. The analysis results for the turbulence model selection will be given in the following paragraphs. For the pressure-velocity coupling, SIMPLE algorithm is selected. As setting the spatial discretization, all the variables except pressure, second order upwind scheme is used and for the pressure, PRESTO! scheme is preferred. The material used in the simulations is air and the air is considered as ideal gas to model compressibility effect.

After deciding mesh size and turbulence model, boundary condition effect is investigated. Former analyses have shown that lip separation occurs at the entrance of S-duct. In order to investigate the effect of this lip separation on AIP profile and to see what would happen unless lip separation exists a hypothetical comparison case is simulated. This case is conducted using uniform profile, which attains the specified mass flow rate, as inlet boundary condition. This way effect of the lip separation on the engine interface plane profile is examined.

At the duct walls, no slip condition is applied and the cut surface of the

numerical domain is treated as symmetry boundary condition. For parameter definitions see Chapter 3.

5.3. Results

Grid refinement study is performed with Realizable-k- ϵ turbulence model that is selected according to its certain mathematical background and ability to give satisfactory results for many engineering fluid mechanics problems. Grid structure is fixed according to the mesh refinement study. Afterwards, computations are conducted using various turbulence models. Numerical studies are finalized with the analysis that uniform inlet mass flow boundary condition is applied instead of numerically obtained inlet velocity profile.

5.3.1. Grid Refinement Study

Top and bottom wall GPR distribution for different mesh sizes is shown in Figures 5.2 and 5.3.

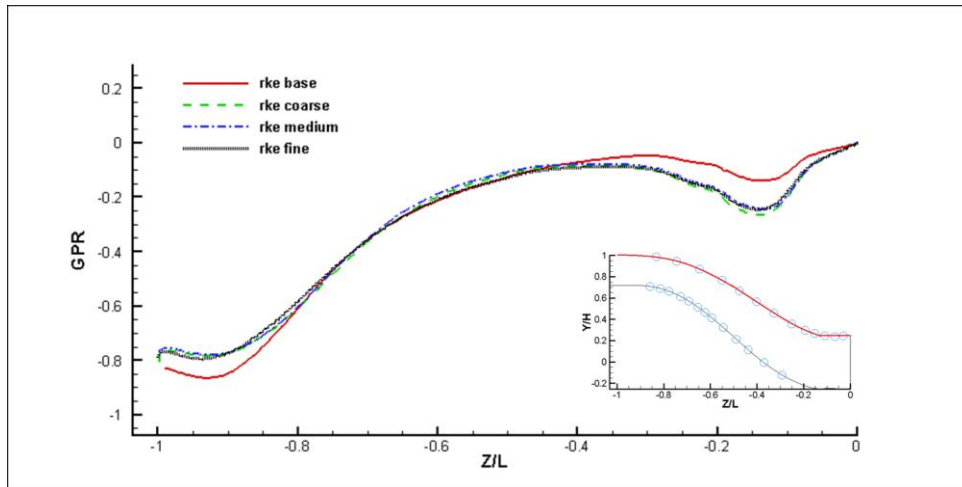


Figure 5.2: Top Wall GPR through the S-duct Diffuser for Grid Optimization

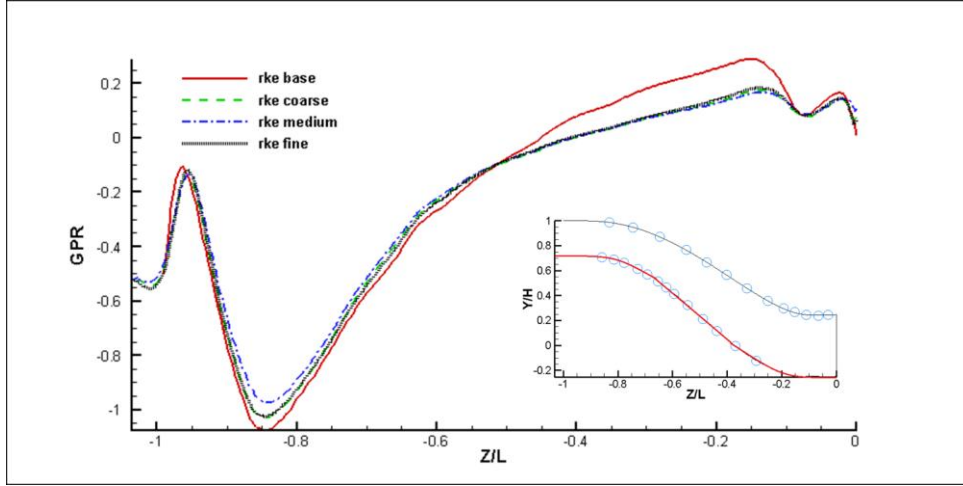
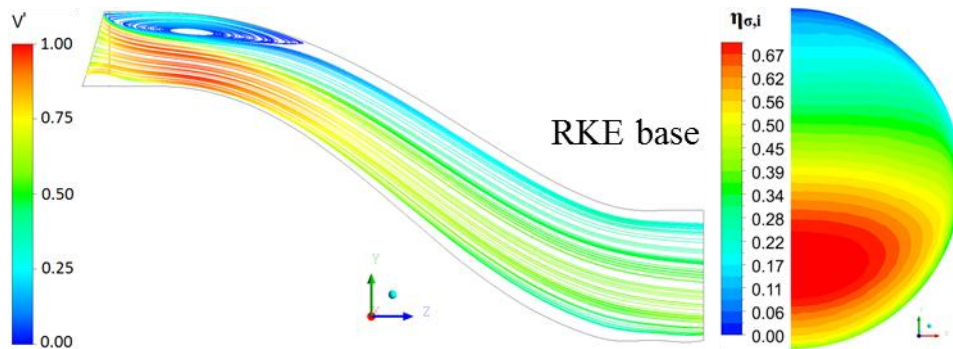


Figure 5.3: Bottom Wall GPR through the S-duct Diffuser for Grid Optimization

In Figure 5.2 and Figure 5.3, it is seen that base solution, which has the coarsest grid structure, is apart from the other computations. Especially the top wall static pressure distribution at the medium RKE and fine RKE solutions are almost coinciding. Hence, it can be concluded that the computations are independent of mesh structure after 3M mesh size. In spite of this fact 4.5M mesh size is kept for the rest of the analyses since the lowest y^+ values are seen at this grid structure. Hence, it is more reliable for near wall solutions.

Symmetry plane streamlines and outlet (η_{σ_i}) contours for the stated analysis are shown in Figure 5.4.



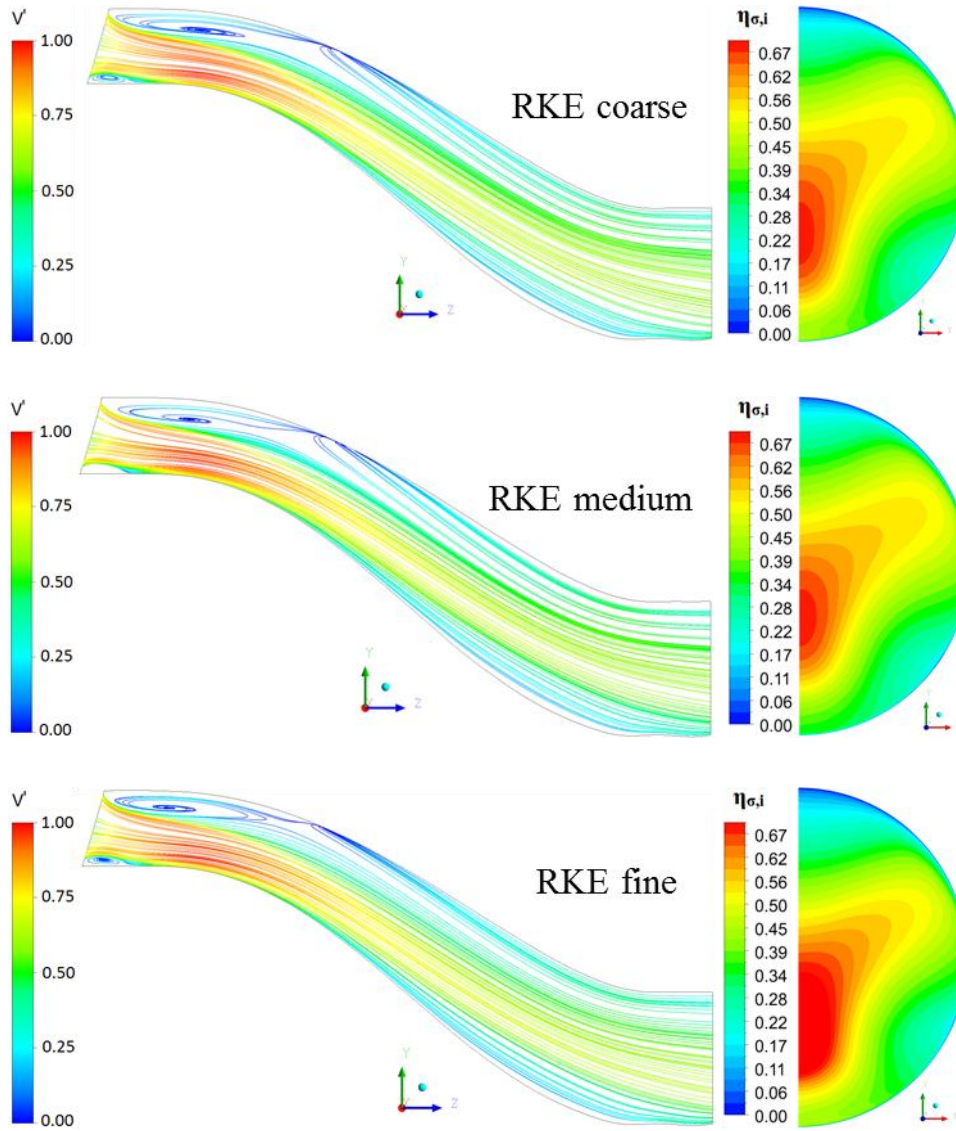


Figure 5.4: Symmetry Plane Streamlines and Outlet η_{σ_i} Contours for Grid Optimization

All of the analyses show similar characteristics. At the symmetry plane reverse flow structures are seen at the top and bottom just after the entrance. At the outlet plane high η_{σ_i} region is seen at the bottom of the plane and low η_{σ_i} region at the top. The top low pressure region occurs as a result of the separation after the second bend. At the other solutions another low pressure region appears at the right bottom and pushes high pressure zone upward. The second low pressure zone comes from the swirling flow.

5.3.2. Turbulence Model Study

Properties of turbulence model study analyses are listed at Table 5.2.

Table 5.2: Turbulence Model Study Analyses Properties

Case	Turbulence model	Mesh size
4	Realizable k- ϵ (RKE)	4682400
5	Spalart – Almaras (SA)	4682400
6	Shear Stress Transport (SST)	4682400
7	Reynolds Stress Model(RSM)	4682400
8	Realizable k- ϵ (uniform mass flow inlet, RKE uni)	4682400

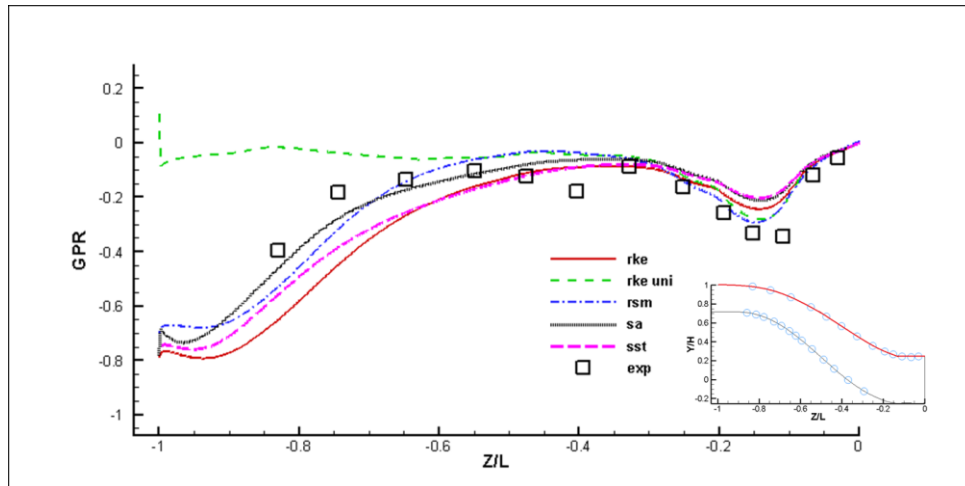


Figure 5.5: Top Wall GPR through the S-duct Diffuser for Different Turbulence Models and BCs

Figure 5.5 compares the top wall GPR measurements against the computations with different turbulence model and uniform inlet profile boundary conditions. All of the computations, except case 8, show similar GPR variation with experiment through the duct length. Low pressure is seen at the entrance because of the lip separation and it increases through the reattachment zone. Then, GPR decreases again as a result of separation because of the second bend. However, they overpredict the pressure drop due to lip separation and underpredict the pressure drop due to second bend separation. Local minimum pressure positions are predicted correctly by numerical analysis; but computations found local maximum GPR position at more upstream. Case 7 finds the local maximum GPR location closest to the experiments. It is seen that uniform inlet profile case (case 8) apart from the test results at the entrance. This is because of the fact that entrance lip separation occurs at the test conditions and it causes the pressure drop as a result. This pressure drop does not appear for the uniform inlet velocity profile. Yet, pressure drop through the second turn is appears for this case also. Numerical results for the bottom symmetry plane show similar results. Pressure drops due to lip separation, first bend separation are remarkable (Figure 5.6).

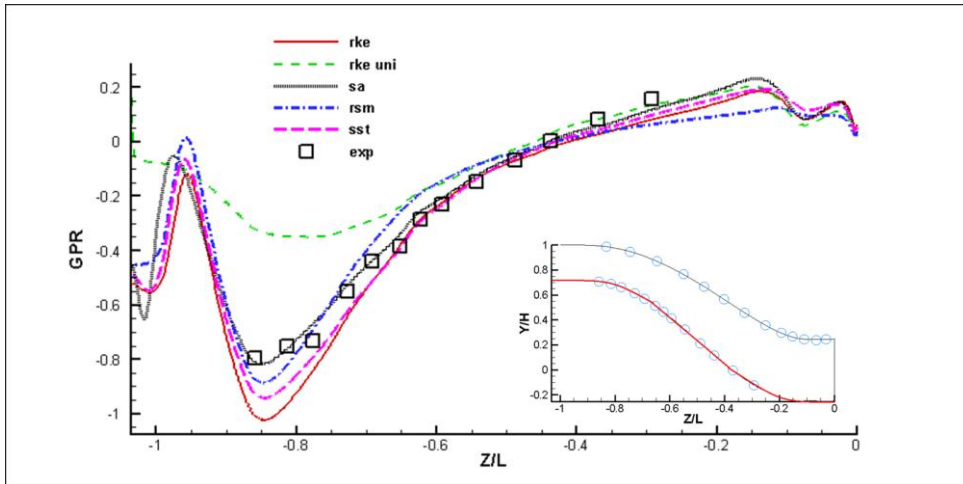
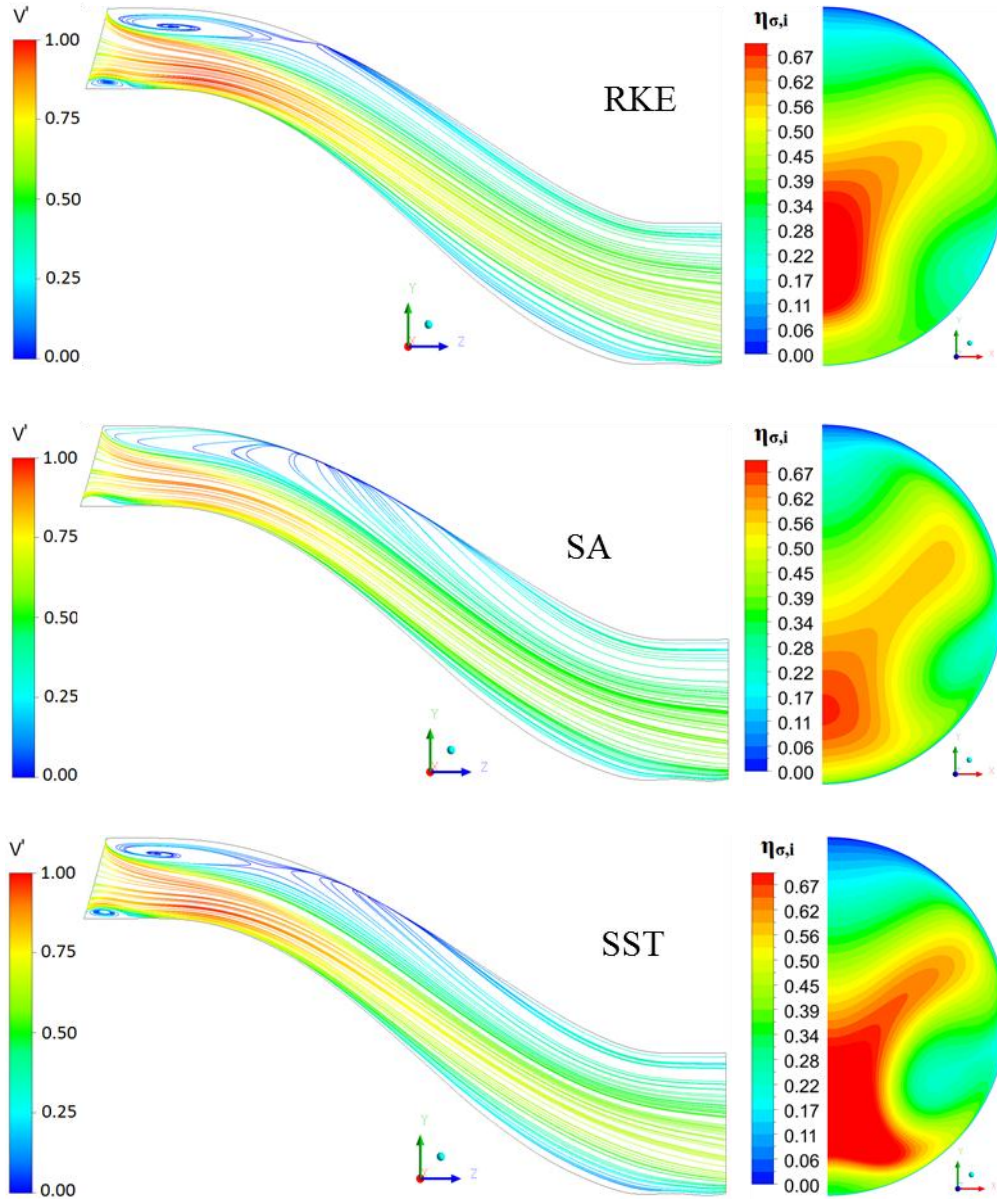


Figure 5.6: Bottom Wall GPR through the S-duct Diffuser for Different Turbulence Models and BCs

Symmetry plane streamlines colored with nondimensional velocity magnitude V' , where $V' = V/V_{max}$, and outlet ($\eta_{\sigma,i}$) contours for different turbulence models are shown in Figure 5.7.



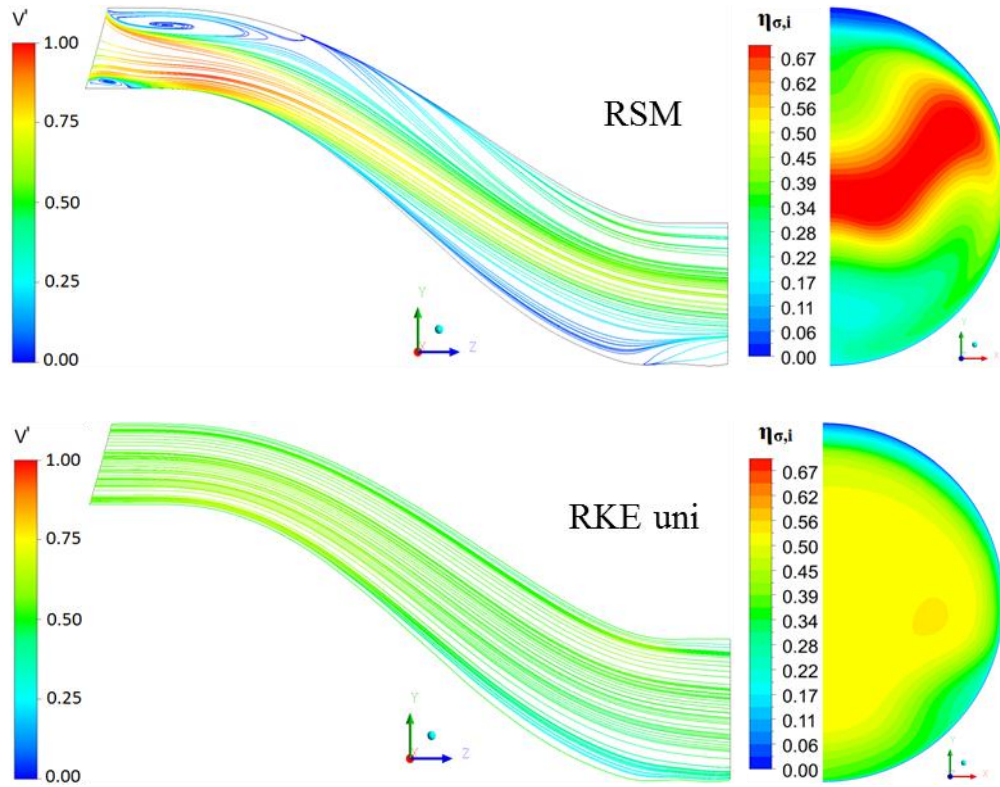


Figure 5.7: Symmetry Plane Streamlines Colored with V' and Outlet η_{σ_i} Contours for Different Turbulence Models and BCs

From Figure 5.7, it is seen that when the entrance profile is uniform, outlet η_{σ_i} profile does not interrupted too much. Also reverse flow does not appear through the symmetry plane streamlines. However, for the separated inlet conditions there are so much flow deviations and this causes outlet pressure distortion. It is seen that unless inlet flow is separated, separations through the turns are weak. Hence, vortexes related to secondary flow are not affecting the flow structure at AIP so much. All of the turbulence models show the lip separation and reattachment regions. However, detachment at the bottom side due to swirl only caught by the Reynolds Stress Model effectively.

Pressure recovery (η_{σ_i}) at the outlet plane obtained from the experiment is shown in Figure 5.8.

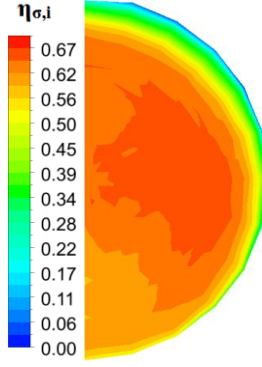


Figure 5.8: Experimental (η_{σ_i}) Contour at the Outlet Plane

The η_{σ_i} contour that obtained from the experiment reveals similar distribution with the RSM computations. However, gradient variations seem smoother at the experiment. It may be interpreted that although RSM model caught the flow structure correctly, it may overpredict the effect of the separations.

Computational results are tabulated in Table 5.3 They are also compared with the experimental results. Parameters are calculated as the area averages at the related planes. Here cases 1-4 shows the grid refinement study as mentioned in table 5.1 while cases 4-8 shows the effect of turbulence model and entrance conditions as mentioned in table 5.2.

Table 5.3: Performance Parameters

Case	\dot{m}/\dot{m}_{\max}	PR	$\eta_{\sigma,i}$	DC(60)
1	1.00	0.9944	0.459	0.235
2	0.99	0.9943	0.442	0.110
3	0.99	0.9943	0.441	0.104
4	0.99	0.9943	0.449	0.150
5	0.99	0.9943	0.447	0.170
6	0.99	0.9945	0.462	0.219
7	0.99	0.9944	0.455	0.146
8	1.00	0.9944	0.455	0.034
Experiment	1.00	0.9954	0.584	0.045

Although computational wall statics pressure values were close to experimental ones; computational performance parameters deviate from the experimental data. It was stated that the outlet η_{σ_i} profile computed using RSM turbulence model was close to the experimental one, however gradients were different. It should be also noted that and there is some surface roughness to be considered because of the manufacturing of the experimental setup by rapid prototyping. In fact, the variations of the performance parameters conclude that also, experimental DC60 calculation is much lower than the numerical values.

In this chapter, flow structure in a diffusing S-duct is numerically investigated. The experimental study that is described in Chapter 3, is simulated and results are compared. Computations are performed with Ansys Fluent 14 commercial CFD code. Various turbulence models are used and their capabilities are compared. Furthermore, effect of the inlet boundary profile is surveyed.

Lip separation is seen at the entrance of the duct. Also, streamwise flow separation regions were caught through the bends of the diffuser. Flow separation is one of the main contributors of pressure loss with secondary flows. Secondary flow structure is appeared as a result of spatial pressure variation. Pressure loss and distortion is seen at the aerodynamic interface plane. It is found that lip separation strengthens the effect of the wall separations inside the duct and increases the AIP distortion drastically.

Numerical analyses approach the experimental wall pressure values considerably well. Also, effect of wall separation and secondary flows at the AIP is caught by the analyses. Reynolds Stress Model gives the closest results to the ones experimentally obtained. However, numerical analyses overpredict the pressure loss and pressure gradient across the AIP.

CHAPTER 6

NUMERICAL INVESTIGATION OF THE TRANSIENT FLOW STRUCTURE IN S-DUCT DIFFUSER

Transient flow structure in an S-duct diffuser that was designed for a micro turbojet engine powered aircraft is investigated. The case was the same with the one described in chapters 3 and 5. In chapter 5, results of RANS computations are compared with experimental data that presented in chapter 3. However, apparent differences are observed between RANS computations and experimental data. The differences are thought to come from the transient characteristics of the flow, which are not being able to be captured by RANS models. Therefore, it is decided to survey the transient structure of the flow using unsteady computational methods. Effectiveness of Unsteady RANS (URANS) and Scale-Adaptive Simulation (SAS) methods are investigated in this chapter.

6.1. Numerical Approach

As in the previous chapter, Ansys Fluent code is used for the unsteady numerical analyses. Since the grid refinement study is concluded in previous chapter, computations are conducted with the decided mesh structure.

The turbulent flow field has been investigated with Pressure-Based solver. In order to capture transient turbulent flow characteristics, URANS-SST and SAS-SST turbulence models are used. For the pressure-velocity coupling, SIMPLE algorithm is selected. As setting the spatial discretization, all the variables

except pressure, second order upwind scheme is used and for the pressure, PRESTO! scheme is preferred.

6.2. Boundary Conditions

The boundary conditions are defined as in Chapter 4. The results of the SST-RANS computations are used as initial conditions. Turbulence fluctuations are triggered using vortex synthesizing approach.

6.3. Turbulence Modeling

Theoretically all RANS models are applicable in unsteady mode; and then they are named as URANS [33]. However, classical URANS models are incapable of providing accurate spectral information, even if the grid and time step resolution would be sufficient. This is considered to be because of the fact that RANS averaging procedure suppresses the turbulence content in the velocity field. Therefore, URANS models are thought to give proper results only at separated regions where transient frequency is much lower than the turbulence frequency.

The Scale Adaptive Simulation (SAS) is a new kind of approach to URANS models ([33], [34]). SAS models work as standard RANS models for steady state flow solutions; however, they reveal a wide range of turbulence spectrum for certain type of transient flows. Different from the conventional RANS formulations, the SAS model adjusts the turbulence length scale to the local flow inhomogeneities. Local flow length scale in any three dimensional flow is defined with classic boundary layer length scale, which is introduced by von Karman. The von Karman length scale appears explicitly in transport equation of the turbulence model. In this form the model works and gives RANS solutions for stationary flows. On the other hand, for highly transient flows, as seen in large separation zones, eddy viscosity is reduced according to locally resolved vortex sizes that is defined by von Karman length scale. Under these conditions The SAS model resolves turbulence spectrum down to grid limit and avoids typical RANS single mode vortex structure.

In this chapter flow structure in the S-duct is investigated using URANS and SAS approaches. SST is used for turbulence modeling in both calculations. CFL number is set to be less than 1 during the computations. For the given CFL number time step is used as 1×10^{-5} s. Maximum number of iterations for convergence at each time step is limited to 15. Time history of mass flow rate and velocity is monitored globally and at some selected points in order to observe that the flow reaches to statistically stable conditions.

6.4. Results

Transient flow structure in the S-duct is investigated using URANS and SAS approaches. SST is used for turbulence modeling in both calculations.

Unsteady computations are conducted using URANS approach firstly. URANS computations are observed to converge steady state. Symmetry plane streamline structure and outlet η_{σ_i} contours are obtained from URANS computations, and they are shown in Figure 6.1 below.

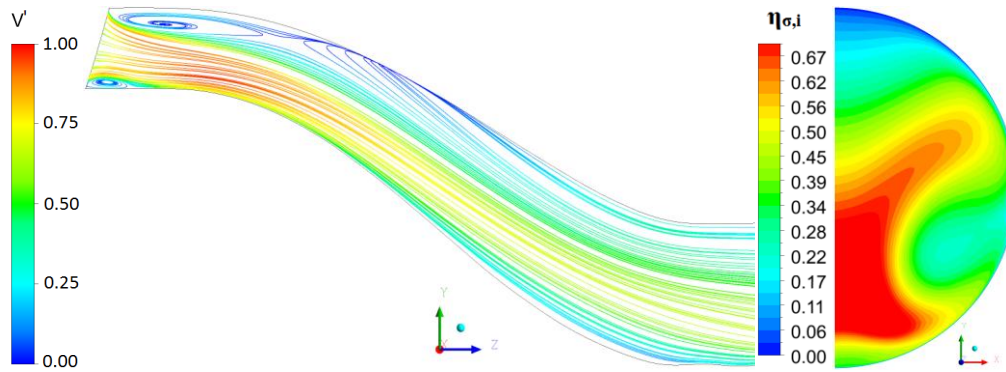


Figure 6.1: Symmetry Plane Streamlines and η_{σ_i} Contours of URANS Analyses

Streamline structure and η_{σ_i} contours of URANS analyses are observed to be almost identical with SST-RANS results that shown in chapter 5. This reveals that the time averaging procedure of RANS approach eliminates turbulence characteristics of the flow. Thus, Unsteady RANS computations are unable to capture the transient structure of the flow.

Afterwards, unsteady computations are continued using SAS approach. SAS computations are seen change instantaneously. Statistics are started to be kept after 0.12s; since the computations are observed to reach statistically steady conditions around that time. History of mass flow rate (\dot{m}/\dot{m}_{\max}) is shown in Figure 6.2. Statistics are kept until 0.5s and then time averages are calculated.

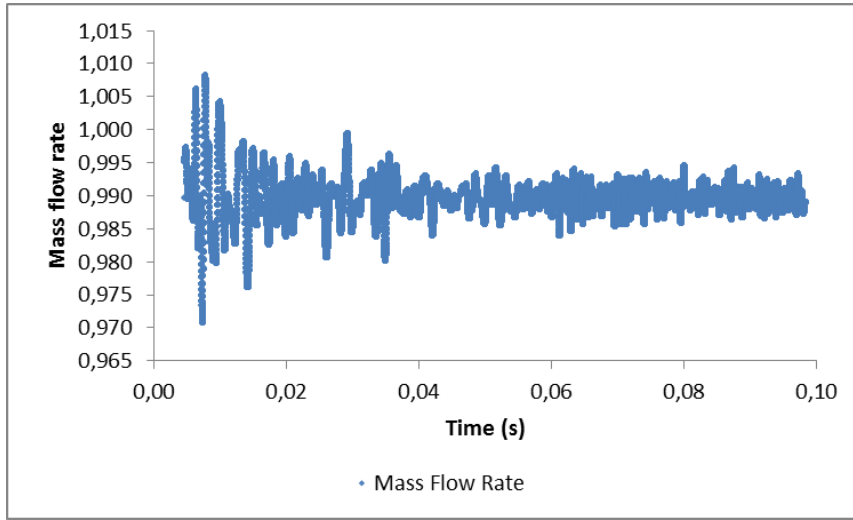


Figure 6.2: Mass Flow Rate (\dot{m}/\dot{m}_{\max}) History

GPR distribution that is obtained from SAS computations is compared with other computational results and also experimental data. Symmetry plane top wall GPR distribution is shown in Figure 6.3 and bottom wall GPR distribution is shown in Figure 6.4.

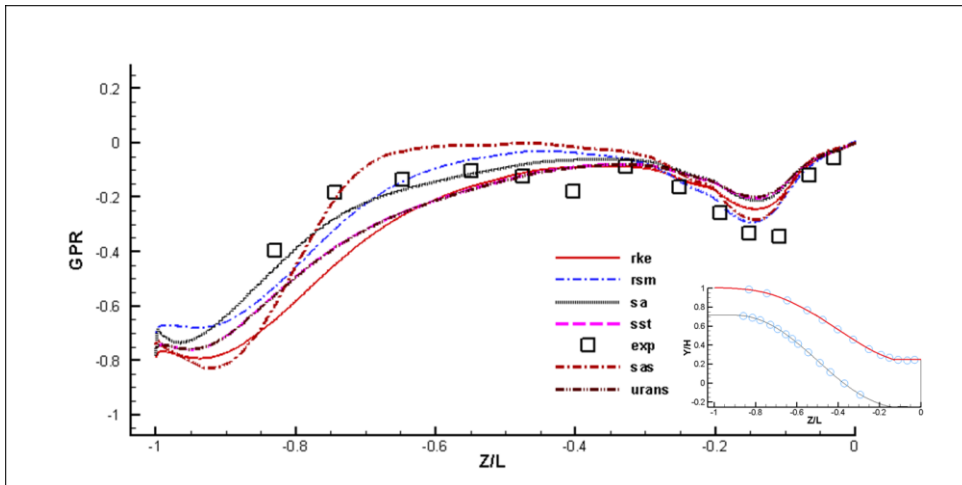


Figure 6.3: Top Wall GPR through the S-duct Diffuser

Figure 6.2 compares the top wall GPR measurements with the computations. Numerical analyses capture the experimental GPR variation through the duct. Low pressure is seen at the entrance because of the lip separation and it increases through the reattachment zone. Then, GPR decreases again as a result of separation because of the second bend. However, computations overpredict the pressure drop due to lip separation and underpredict the pressure drop due to second bend separation. Local minimum pressure positions are predicted correctly by numerical analysis. URANS SST results are almost the same with RANS SST results as streamlines and η_{σ_i} contours. Although SAS analyses also uses SST for turbulence modeling, its results differ from RANS and URANS computations. SAS analyses predicted most accurately the local GPR value that is seen because of second turn. However, it shows more drastic GPR variation after the lip separation and it may be concluded that to predict reattachment region earlier than in real.

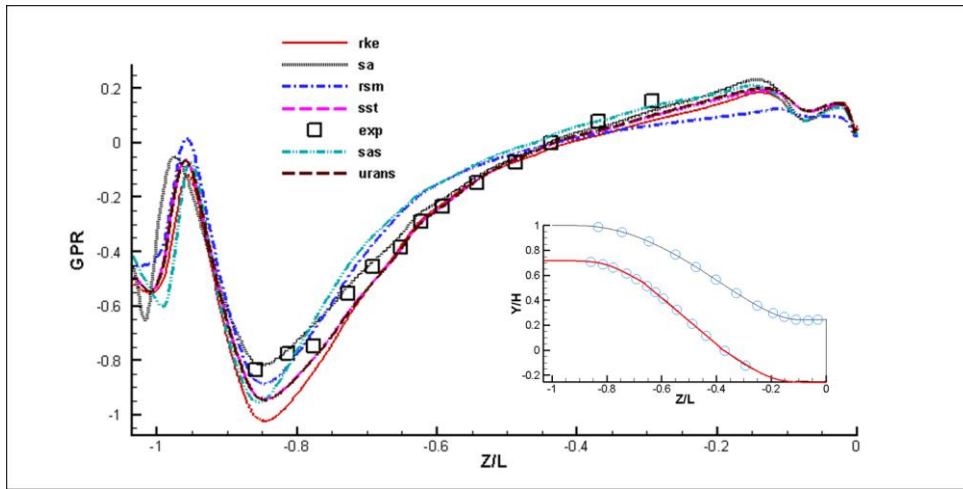
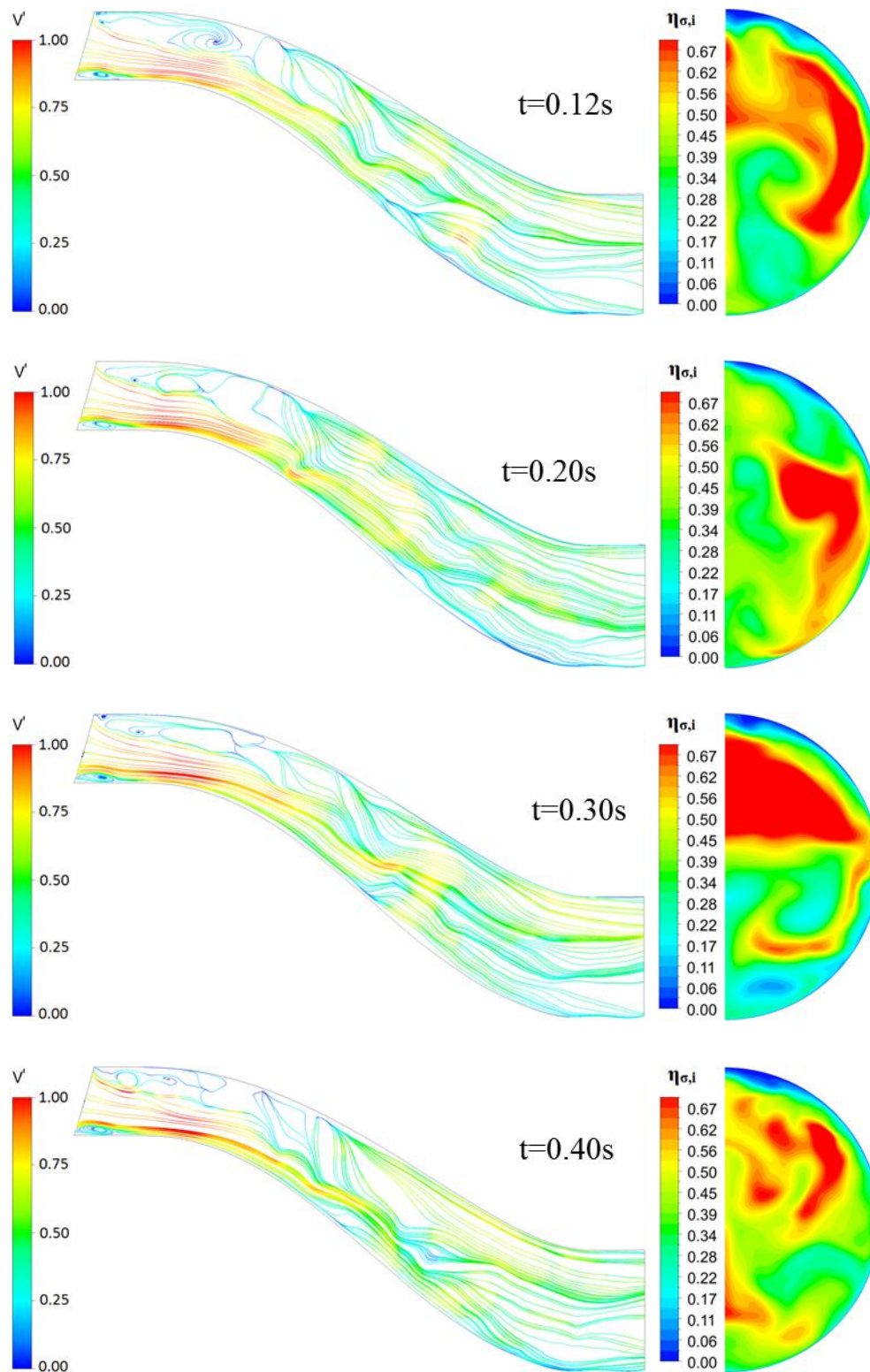


Figure 6.4: Bottom Wall GPR through the S-duct Diffuser

Numerical results for the bottom symmetry plane show similar results. Pressure drops due to lip separation but flow reattaches. Just after the reattachment, GPR drops remarkably due to first bend separation. S-A and RSM models best fit with the experimental data at the first bend. SAS results show some overshoot at the first bend separation and reattachment zone; however, it captures the experimental data most accurately after the reattachment point.

Among results of SAS computations symmetry plane streamlines and outlet pressure recovery contours at different times are shown in Figure 6.4.



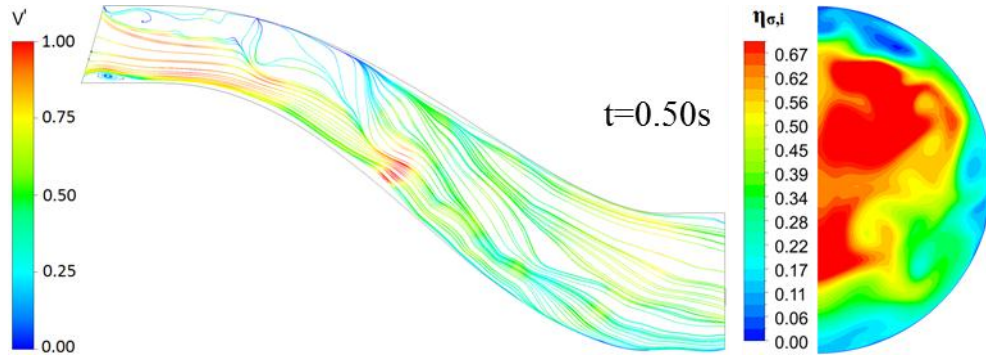


Figure 6.5: Instantaneous Symmetry Plane Streamlines and Outlet η_{σ_i} Contours at Different Times

From Figure 6.4, it is seen that the structure of the flow is changing drastically in time. Time averaging procedure of RANS suppresses the effect of turbulence fluctuations and this may be the reason why results of RANS solutions for outlet η_{σ_i} distribution are different from the experimental data.

Time averaged η_{σ_i} contours that obtained from the SAS computations are shown in Figure 6.5. Moreover, experimental η_{σ_i} contours are also shown for comparison.

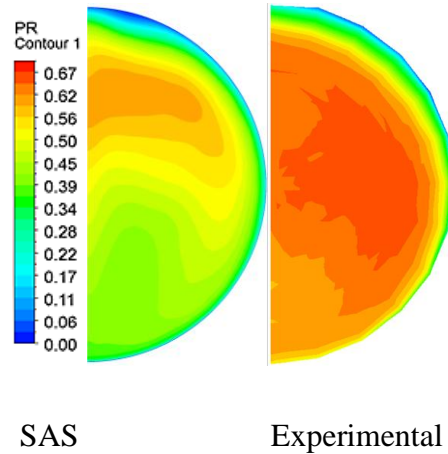


Figure 6.6: η_{σ_i} Contours of SAS Analyses and Experiment

In Figure 6.5 lower pressure region is seen at the bottom in both SAS analyses and experiment. This is expected because of the swirl. Furthermore, pressure deficiency is seen at the top region as well. Pressure drop at this region is

expected because of the separation due to second turn. This deficiency zones are seen in both experiment and SAS analyses. These variations were also observed in other RANS calculations; but the difference between the maximum and minimum magnitude of the η_{σ_i} through the area were greater.

Although characteristics of the η_{σ_i} variation through the area is seen similar for SAS analyses and experiment; magnitude of the η_{σ_i} gradient through the area and expansion of these zones vary. Therefore, compatibility parameters that defined in Chapter 3 are used to quantify flow characteristics.

Computational results are tabulated in Table 6.1. They are also compared with the experimental results. Parameters are calculated as the area averages at the related planes. Here cases 4-7 shows the RANS analyses as mentioned in table 5.2.

Table 6.1: Performance Parameters

Case	\dot{m}/\dot{m}_{\max}	PR	$\eta_{\sigma,i}$	DC(60)
4	0.99	0.9943	0.449	0.150
5	0.99	0.9943	0.447	0.170
6	0.99	0.9945	0.462	0.219
7	0.99	0.9944	0.455	0.146
URANS SST	0.99	0.9945	0.462	0.232
SAS SST	0.99	0.9945	0.462	0.056
Experiment	1.00	0.9954	0.583	0.045

Although wall static pressure values obtained from numerical calculations were close to experimental values, there is a level of difference between computed performance parameters of RANS and URANS and experimental ones. The difference may be caused by the unsteady characteristics of the internal swirling flow and RANS based analyses provide limited capability to resolve that phenomena.

In fact, the time dependent variation of the flow structure is shown with the SAS calculations and results of this approach were much closer to the experimental data. This shows that the SAS-SST models are more successful to resolve highly transient separated swirling flows as in this case. However, they are still RANS based models and have limitations based on that.

Computational source is an important issue for numerical analyses. Whereas SAS offer much better results than URANS, it consumes more time also. In this study both URANS and SAS analyses are conducted using 8 number of CPU as computational source. CFL number is chosen to be less than 1 and time step is used as 1×10^{-5} seconds. With this capability URANS computations took 4 days, while SAS needed 6 weeks for 0.5s (24 flow through time) computational time. Even though the SAS requires a good computational source, results are not perfectly match with experiments. Therefore, to achieve better results Large Eddy Simulation (LES) approach may be considered if there is sufficient computing source and time.

CHAPTER 7

CONCLUSION

In this study, flow structure in a diffusing S-duct is investigated using experimental and numerical methods.

Previous experimental and computational studies have been conducted to determine the characteristics of the fluid motion within S-duct diffusers. In the accessible literature, reviewed studies similar to the present study from the viewpoint of objectives are discussed. It is seen that the flow in S-duct air inlets is subject to two main phenomena, which cause the loss of performance and distortion at the compressor face: boundary layer separation and secondary flows.

Experiments are performed at three different mass flow rates. Using wall static pressure measurements separation regions were caught through the first and second bends of the S-duct diffuser. Flow separation is observed as one of the main contributors of pressure loss with secondary flows. Total pressure loss is seen to increase with increasing mass flow rate. Furthermore, circumferential distortion is also examined.

Flow structure in a short, diffusing S-duct inlet is numerically investigated. Computations are compared with the experimental data obtained from the study conducted at RAE facilities for numerical validation. RANS solutions have been computed with freestream Mach number fixed at 0.207 and Reynolds number based on the non-dimensional engine face diameter of 777,000. The

results were found to compare well with experiment. SST turbulence model gives the most suitable results considering mass flow rate, Mach number and pressure recovery values together.

Highest mass flow rate experimental case that is described in Chapter 3 is simulated and results are compared with the experimental data. Computations are performed with Ansys Fluent 14 commercial CFD code. Various turbulence models are used and their efficiencies are compared. Furthermore, effect of the inlet boundary profile is surveyed. Lip separation is seen at the entrance of the duct. Also, streamwise flow separation regions were caught through the bends of the diffuser. Flow separation is one of the main contributors of pressure loss with secondary flows. Secondary flow structure is appeared as a result of spatial pressure variation. Pressure loss and distortion is seen at the aerodynamic interface plane. It is found that lip separation strengthens the effect of the wall separations inside the duct and increases the AIP distortion drastically.

Numerical analyses approach the experimental wall pressure values considerably well. Also, effect of wall separation and secondary flows at the AIP is caught by the analyses. Reynolds Stress Model gives the closest results to the ones experimentally obtained. However, numerical analyses overpredict the pressure loss and pressure gradient across the AIP.

Afterwards, transient analyses are performed for the same case using URANS and SAS approaches. While results of URANS computations are almost identical with RANS results, SAS analyses provide impressive improvement especially for predicting DC60 parameter. This shows that the SAS-SST models are more successful than RANS to resolve highly transient separated swirling flows as in this case.

Although, SAS computations have shown impressive improvement to capture the AIP flow structure; the computational results still do not perfectly match with the experiments. This case can be surveyed using LES approach in the future when sufficient computational source is available. Moreover, the internal

velocity field can be investigated in detail using PIV with the improvements of the test setup.

In order to reduce the losses and distortion at the engine face, length-to-height ratio of the S-duct diffuser may be increased. However, most of the time geometrical parameters are strictly constrained. In that case, the use of active and passive flow control techniques may be an option in order to reduce the separation and secondary flow structures as observed in this study.

REFERENCES:

- [1] Seddon, J., & Goldsmith, E. (1985). *Intake aerodynamics: An account of the mechanics of flow in and around the air intakes of turbine-engined and ramjet aircraft and missiles*. London: Collins.
- [2] Goldsmith, E. (1993). *Practical intake aerodynamic design*. Washington, DC: American Institute of Aeronautics and Astronautics.
- [3] General Electric Company Flight Propulsion Division (1951). *Installation Handbook for Turbojet Engines*. Evendale, Ohio, Aircraft Gas Turbine Division, General Electric.
- [4] Luers, A. S. (2003). *Flow Control Techniques in a Serpentine Inlet: An Enabling Technology to Increase the Military Viability of Unmanned Air* (Unpublished master dissertation). Massachusetts Institute of Technology, Cambridge, Massachusetts.
- [5] Harrison, N. A. (2005). *Active Flow Control of a Boundary Layer Ingesting Serpentine Diffuser* (Unpublished master dissertation). Virginia Polytechnic Institute and State University, Blacksburg, Virginia.
- [6] Bissinger, N. C. and Breuer, T. (2010). Basic Principles – Gas Turbine Compatibility – Intake Aerodynamic Aspects. *Encyclopedia of Aerospace Engineering*.
- [7] Wellborn, S. R., Reichert, B. A., and Okiishi, T. H., “An Experimental Investigation of the Flow in a Diffusing S-Duct,” 28th Joint Propulsion Conference and Exhibit. 6-8 July 1992, Nashville, Tennessee, AIAA-92-3622
- [8] Brear, M. J., Warfield, Z., Mangus, J. F., Braddom, S., Paduano, J. D., & Philhower, J. S. (2004). Flow separation within the engine inlet of an uninhabited combat air vehicle (UCAV). *Journal of Fluids Engineering*, (2), 266.

- [9] Anabtawi, A.J., (1999). *Experimental Investigation of Boundary Layer Ingestion into Diffusing Inlets* (Doctoral dissertation). Retrieved from ProQuest Dissertations and Theses (9955053)

- [10] Berger, S. A., Talbot, L., & Yao, S. (1983). Flow in curved pipes. *Annual Review of Fluid Mechanics*, 15, 461-512. doi:10.1146/annurev.fl.15.010183.002333

- [11] Sullivan, J., “Active Flow Control of Secondary Flows in Engine Inlets” Purdue University (AFOSR 49620-02-1-0123 / Purdue 531 1282-0171)

- [12] Gerolymos, G., Vallet, I., Joly, S., & Mallet, M. (2010). Reynolds-stress model flow prediction in aircraft-engine intake double-S-shaped duct. *Journal of Aircraft*, 47(4), 1368-1381. doi:10.2514/1.47538

- [13] Harrison, N., Anderson, J., Fleming, J., & Ng, W. (2013). Active flow control of a boundary layer-ingesting serpentine inlet diffuser. *Journal Of Aircraft*, 50(1), 262-271. doi:10.2514/1.C031818

- [14] Hercock, R. G., (1982) Effects of Intake flow on engine stability. Paper 20 AGARD CP 324

- [15] Hawkins, J. E. (1976). YF-16 inlet design and performance. *Journal Of Aircraft*, 13436-441

- [16] “Air Intakes for High Speed Vehicles”, AGARD-AR-270, September 1991

- [17] Vakili, A .D. Wu, J. M. Liver P. and Bhat, M. K., “Experimental Investigation of Secondary Flow in a Diffusing S- Duct,” University of Tennessee Space Institute, Report No. TRUTSI 86/14, University of Tennessee, Tullahoma, TN, (1984).

- [18] Harloff, G. J., Reichert, B. A., and Wellborn, S. R., "Navier-Stokes Analysis and Experimental Data Comparison of Compressible Flow in a Diffusing S-Duct," AIAA Paper 92-2699, 1992.

- [19] Harloff, G. J., Reichert, B. A., and Wellborn, S. R., "Navier-Stokes Analysis and Experimental Data Comparison of Compressible Flow in a Diffusing S-Duct," 13th International Conference on Numerical Methods in Fluid Dynamics. 6-10 July 1992, Rome, Italy, AIAA-92-3622
- [20] Wellborn, S. R., Reichert, B. A., and Okiishi, T. H., A Study of the Compressible Flow Through a Diffusing S-Duct, Washington, D.C.: National Aeronautics and Space Administrations, NASA TM-10641, December 1993
- [21] Wellborn, S. R., Reichert, B. A., & Okiishi, T. H. (1994). Study of the compressible flow in a diffusing S-duct. *Journal Of Propulsion And Power*, 10(5), 668-675.
- [22] Tindell, R. (1988). Highly compact inlet diffuser technology. *Journal Of Propulsion And Power*, 4(6), 557-563.
- [23] Kirk, A., Gargoloff, J., Rediniotis, O., & Cizmas, P. (2009). Numerical and experimental investigation of a serpentine inlet duct. *International Journal Of Computational Fluid Dynamics*, 23(3), 245-258. doi:10.1080/10618560902835558
- [24] Kirk, A.M., (2006). *Active Flow Control in an Advanced Serpentine Jet Engine Inlet Duct*. (Unpublished master's thesis). Texas A&M University, College Station, Texas.
- [25] Fiola, C., & Agarwal, R. K. (2014). Simulation of secondary and separated flow in a diffusing S-duct using four different turbulence models. *Proceedings Of The Institution Of Mechanical Engineers -- Part G -- Journal Of Aerospace Engineering (Sage Publications, Ltd.)*, 228(11), 1954. doi:10.1177/0954410013507249
- [26] Fiola, C., (2013). *Numerical Simulation of Separated and Secondary Flows in Diffusing S-Ducts for Air Breathing Propulsion* (Master dissertation). Retrieved from Electronic Theses and Dissertations. (1168)

- [27] Menzies, Ryan D.D. (2002) *Investigation of S-shaped Intake Aerodynamics Using Computational Fluid Dynamics* (PhD thesis) Retrieved from <http://theses.gla.ac.uk/id/eprint/1440>
- [28] Aslan, S., Yilmazturk, S., Kurtulus, D. F. “Aerodynamic Investigation of a Serpentine Inlet Designed for a Micro-Turbojet Engine Powered Aircraft” 1st International Symposium of Sustainable Aviation. 31 May- 3 June 2015, Istanbul, Turkey, ISSA-2015-129
- [29] “Application of CFD to High Offset Intake Diffusers”, GARTEUR AD/AG-43, October 2012
- [30] Wendt, J. F., & Anderson, J. D. (2009). *Computational fluid dynamics: An introduction* (3rd ed., pp. 15-51). Berlin: Springer.
- [31] ANSYS Fluent User Manual
- [32] Reynolds, Osborne, 1895: "On the Dynamical Theory of Incompressible Viscous Fluids and the Determination of the Criterion." *Philosophical Transactions of the Royal Society of London. A*, v. 186, pp. 123-164. Available online from JSTOR.
- [33] Egorov, Y., and Menter, F., Development and Application of SST-SAS Turbulence Model in the DESIDER Project
- [34] Davidson, L., “Evaluation of the SST-SAS Model: Channel Flow, Asymmetric Diffuser and Axi-symmetric Hill,” European Conference on Computational Fluid Dynamics, 2006, The Netherlands